Experimental investigation of the heat generation rate of a large format pouch-type lithium-ion battery

by

Munnyeong Choi

A thesis submitted to the Graduate Faculty of
Auburn University
in partial fulfillment of the
requirements for the Degree of
Master of Science

Auburn, Alabama
December 10, 2022

Keywords: Lithium-ion battery, battery thermal management system, heat generation, thermal model, entropy coefficient

Approved by

Song-Yul Choe, Chair, Professor of Mechanical Engineering
Dan Marghitu, Professor of Mechanical Engineering
Nicholas Tsolas, Professor of Mechanical Engineering

Abstract

When battery cells are charged and discharged, heat is generated because of chemical reactions and the associated charge transport. The heat should be appropriately rejected to ensure the performance, safety, and lifespan of the lithium-ion battery. In fact, the performance of the cell varies dramatically with temperature, and cycle life can be extended if the operating temperature window is well maintained by a thermal management system (TMS) that properly rejects the heat and controls the temperature of the cell. For optimal design of such a TMS, understanding of the heat source terms, generating, and releasing mechanisms are required.

The heat generation during battery operation is largely dominated by irreversible and reversible heat. The irreversible heat is governed by the cell's internal resistance, while the reversible heat is governed by the entropy coefficient. Hence, to accurately predict the total heat generation rate (HGR), the resistance and entropy coefficient must be measured as a function of State of Charge (SOC) and temperature. An isothermal calorimeter is developed using thermoelectric assemblies (TEAs) to measure the thermal parameters of large format pouch-type lithium-ion batteries at different operating conditions.

Entropy coefficient (EC) was experimentally measured with a 109 Ah capacity large format pouch cell with an NMCA cathode and graphite-SiO_x composite anode. The hysteresis phenomenon was observed between charging and discharging EC. The operating temperature has a negligible effect on EC over the entire SOC and temperature range considered (0-45^{o}C). Furthermore, the effect of C rate and temperature on HGR is considered. As the C rate increases, the total HGR increases proportionally, and irreversible heat becomes the dominant part. Additionally, as the temperature decreases, the HGR rapidly increases due to the internal resistance

increases. The experimentally measured data are compared with the HGR calculated by the thermal model, and the result has a good agreement.

Acknowledgements

I would like to express my deepest appreciation to my advisor, Dr. Song-Yul Choe, for his continuous support of this research and his patience, motivation, and immense knowledge. His guidance helped me in all the time of research and writing of this thesis.

My deep appreciation goes to the committee members, Professor Dan Marghitu and Professor Nicholas Tsolas, for their encouragement, insightful comments, and suggestions in developing this research. I also sincerely thank to my research team members: Dr. Yang Hu, Dr. Minseok Song, Ms. Kyungjin Yu, Mr. Xiaoniu Du, Mr. Junbeom Park, Mr. James Choi, and Mr. Adekanmi Adeyinka for the stimulating discussions and cherished time spent together in the lab. Lastly, I would like to express gratitude to my family and friends for their encouragement and emotional support.

Table of Contents

List of Tables

List of Figures

List of Symbols

A	Sandwich area of the cell (cm^2) / contact area (m^2)
C	Heat capacity (k J kg^{-1} K^{-1})
E	Open circuit voltage (V)
F	Faraday constant (96,487 C mol^{-1})
f	Frequency (Hz)
h	Convection transfer coefficient (W m^{-2} K^{-1})
I	Applied current (A)
L	Length of a cell (mm)
Q	Capacity of the cell (Ah) / heat energy (J)
$\dot{Q}$	Heat generation rate (W)
R	Resistance (Ω)
T	Cell temperature (K or °C) / thickness of a cell (mm)
t	Time (s)
U	Equilibrium potential (V)
U_{OC}	Open circuit voltage (V)
V	Voltage (V)
W	Width of a cell (mm)
Z	Impedance (Ω)

Greek symbols

ϕ	Phase angle (degrees or radians)
ρ	Cell density (kg m^{-3})
η	Energy efficiency

Subscripts and Superscripts

amb	Ambient
ch	Charge
dch	Discharge
elec	Electric
f	final
irr	Irreversible
init	Initialmea Measurable
n	Negative electrode
p	Positive electrode
ref	Reference
rev	Reversible

List of Abbreviations

AC	Alternating Current
CC	Constant Current
BMS	Battery Management Systems
CV	Constant Voltage
CE	Coulometric Efficiency
DAQ	Data Acquisition system
DOD	Depth Of Discharge
EC	Entropy Coefficient
ECM	Equivalent circuit model
EV	Electric Vehicle
EIS	Electrochemical Impedance Spectroscopy
ETCR	Equivalent temperature change rate
HEV	Hybrid Electric Vehicle
HGR	Heat Generation Rate
HPPC	Hybrid pulse power characterization
HTFDA	Hybridized Time-Frequency Domain Analysis
IHC	Isothermal heat conduction calorimetry
LIB	Lithium Ion Battery
OCV	Open Circuit Voltage
PLC	Programmable logic controller
SEI	Solid Electrolyte Interface

SOC	State Of Charge
SOH	State Of Health
TMS	Thermal Management System
TEM	Thermoelectric Module
TEA	Thermoelectric Assembly
UDDS	Urban Dynamometer Driving Schedule

1. Introduction

1.1 Background of research

High global population growth rates and the associated industrialization have triggered to a rapid increase in energy consumption. 80% of global energy consumption is covered by fossil fuels, which results in severe environmental concerns including ozone depletion, greenhouse gas emissions, and climate change [1]. Particularly, the dramatic climate change of the earth has led to concerted efforts by several countries of the world aiming to keep the global temperature within the 1.5^{o}C threshold [2]. In fact, the transport sector has a higher reliance on fossil fuels than any other sectors and accounts for 37% of CO_2 emissions [3]. 87% of the world's CO_2 emissions from the transportation sector comes from ground transport [4]. The best response to combat these emissions in the transport sector is to seek alternative power sources for automobiles, airplanes, trains and so on, etc. This has led to development of alternative power sources that are energy efficient and clean, especially for Electric Vehicles (EV) and Hybrid Electric Vehicles (HEV) that need the increased energy storage devices. Over the years, lithium-ion batteries have accepted due to their long cycling life, high power and energy density, low self-discharge, and wide operating temperature range.

The lithium-ion battery has revolutionized the industry. It has become the energy storage media of choice for portable devices, grid storage, and electric vehicles. However, a wide adoption of lithium-ion batteries (LiBs) in EVs is limited by range anxiety and prolonged charging time. The performance of LiB is dependent on several factors, such as C rate, operating temperature and other operation conditions. Also, LiBs generate heat during operation due to charge transport and chemical reactions. A significant amount of the heat is rejected by the cooling system or transferred

to the ambient, but the remaining heat increases the cell temperature. This is detrimental to the performance of the cell. The effect of internal heat generation on the cell performance is prominent under abusive conditions such as low temperature and high Crates. For instance, charging at subzero temperatures leads to formation of lithium plating that results in impedance rise, and internal short circuits that may eventually cause serious thermal runaway and explosion . Therefore, the operating temperature of the cell must be actively managed to mitigate the safety issues associated with LiB operations. An efficient battery thermal management system must be developed to reject the heat generate, so the battery temperature is controlled, allowing the battery to operate safely.

Understanding the thermal characteristics, heat generation behaviors of the cells under various operating situations with different charge or discharge rates, SOC, and ambient temperatures, is the crucial factor for a cost-effective and efficient design of the TMS [5]. Many researchers have recently attempted to characterize the heat generation in the cell and explore the accompanying mechanisms [6]. One of the approaches is the determination of heat generation rate from the temperatures measured during operation using thermal sensors such as thermocouples, thermistors, resistance temperature detectors, and thermal infrared cameras, where the heat generation rate and the related heat source terms are computed using the energy equation from the measured temperature responses. Although the approaches need simple hardware configuration, their accuracy is mostly dependent on the accuracy of the developed energy equation and suppression of the high frequent noises. Another drawback is inaccurate capture of the internal thermal behavior by the cell surface temperature.

The heat generation rate of LiBs can be measured using specially designed calorimeter such as accelerated rate calorimetry (ARC) and isothermal heat conduction calorimetry (IHC). The

ARC simulates an adiabatic environment, while the IHC promotes a constant temperature during the measurement. Although the equipment is costly, both methods provide the sufficient capability for accurate and dynamic measurements of HGR. However, the equipment is pretty expensive, and space for the placement of cells is limited [7].

Therefore, several different low-cost calorimeter types have been proposed that allow for measurement of the HGR of large-format pouch type lithium-ion batteries. Chen et al. [8] estimated the HGR of a prismatic cell by wrapping the cell with a thermally stable material and putting it in a room with a constant temperature. Since the temperature of the cell is not actively controlled, the cell's temperature can vary during the tests, which causes errors and in turn decreases the accuracy of the measurements. Yin et al. (2017) used two thermoelectric modules (TEMs) with a closed loop controller to regulate the surface temperature of the cell. The HGR is directly estimated by a Kalman filter with a simplified heat transfer model of the TEM [9]. Ahmad et al. [7] developed a cost-effective isoperibolic calorimeter to mitigate the concerns related to the high cost of the commercially available calorimeter. In contrast to the isothermal calorimeter, which uses a constant temperature of the reaction system, the isoperibolic method uses a constant ambient temperature. With the specially designed calorimeter, they were able to create a constant temperature environment for fast determination of entropy-variation of LiBs.

1.2 Scope of research

A pack is mechanically made of assembled cells with cooling fins under compressing pressures, where surface temperatures of the cell are not uniform due to the large size of cells. LiB performance is strongly affected by operating surface temperature and pressures.

Therefore, understanding of heat generation is crucial to develop an efficient battery thermal management system, which rejects the heat generated during the electrochemical processes occurring in cells and allows the battery to operate safely. The scope of this research is to experimentally investigate the thermal behaviors of the large format pouch type of a cell at different operating conditions.

1.3 Contribution to knowledge

In Li-ion batteries, whether pouch, cylindrical or prismatic, heat can dissipate at some locations more easily than from others. For example, the poor through-plane conductivity of battery materials such as polymer separators causes higher heat accumulation in the core compared to the regions closer to the surface [10]. The heat generated during operation increases the temperature of the cell, which is detrimental to the performance of the cell. Furthermore, the current densities and the heat generation rates are unequal at different locations. The non-uniform current distribution causes excessive plating in the wormer region. Thermal gradients between the electrodes are observed. Lithium plating is reduced if the temperature for anode is higher than for cathode. In contrast, If the temperature for cathode is higher than for anode, lithium plating is exacerbated [11]. Additionally, low temperature operation leads to lower energy efficiency and more heat generation due to the higher overpotential resulting from the increased transport limitations and slower kinetics. On the other hand, high temperature operation leads to increased growth of the Solid-Electrolyte interface (SEI) layer on the anode, binder decomposition, metal dissolution, and phase transition. This causes loss of lithium inventory (LLI), loss of active material (LAM) and Conductivity Loss (CL).

To characterize the effect of temperature accurately, a method of battery temperature control needs to be developed such that battery temperature can be kept a constant regardless of loading currents and the associated internal heat generation. The assessment of temperature effects on battery characteristics highlights the importance of developing an effective thermal management system to keep the batteries at an ideal operating temperature. The design of such a system requires accurate knowledge of the heat generation rates of Li-ion batteries at varying operating temperatures and discharge conditions. Accurate modeling of the heat generation of the batteries is very challenging due to the complex mechanisms involved in heat generation and electrochemical mechanisms. Hence, an experimental investigation is needed to accurately characterize the heat generation rates of the battery at various operating conditions to examine the effects of operating conditions.

1.4 Thesis outline

The basic structure of the thesis is shown as follows;

- Chapter 1 discusses the background of the study, research motivation and objectives, research scope, and contribution to knowledge. The thesis briefly introduces the basic principle of lithium-ion batteries during charging and discharging with chemical reactions and identifies the thermal effect on the battery.
- Chapter 2 reviews design of lithium-ion battery and its working principle. The heat source terms are introduced in this chapter, and the experimental procedure for determining reversible and irreversible heat sources is discussed.

- Chapter 3 overviews the experimental setup for the thermal characterization of a lithium battery. The hardware and software parts of the designed test station are briefly described, and the procedure for measuring HGRs and entropy coefficient are described.
- Chapter 4 presents the results of the measurement of HGR using a multifunctional calorimeter and then compared with a simple thermal model. Also, the entropy coefficient (EC) as a function of SOC was determined using hybridized time-frequency domain analysis (HTFDA) method. The effects of cell chemistry, operating temperature, charge and discharge, and capacity fade on EC are analyzed.
- Chapter 5 includes concluding remarks and discusses future work.

2. Literature Review

2.1 Review of different battery chemistries

In the world, increasing toxic emissions from the tailpipe of diesel and petrol cars have caused air pollution problems. To reduce the environmental impact of motor vehicles, the use of HEVs or EVs has been developed. Governments are providing various incentives to consumers to adopt more energy efficient electric vehicles that need electric energy storage. The battery is the solution because of its high charge/discharge efficiency and energy density. Different battery chemistries, such as Nickel-cadmium (NiCd), Nickel-metal Hydride (NiMH), Lead-Acid, and Lithium-ion, have been developed.

NiCd batteries have been commercially used since 1950. Although the long cycle life, there are limitations such as relatively low energy density and high self-discharge rate. The chemical reactions of the nickel-cadmium batteries are as below [12];

The chemical reactions on the negative electrode are

$$2(OH)^{-} + Cd \rightleftharpoons Cd(OH)_2 + 2e^{-} \tag{2.1}$$

The chemical reactions on the positive electrode are

$$2NiOOH + 2H_2O + 2e^{-} \rightleftharpoons 2Ni(OH)_2 + 2OH^{-} \tag{2.2}$$

The overall chemical reactions of NiCd batteries are

$$2NiOOH + 2H_2O + Cd \rightleftharpoons 2Ni(OH)_2 + Cd(OH)_2 \tag{2.3}$$

Since then, Nickel-metal Hydride battery has been in common use since 1990. It contains only mild toxins and has a 30-40 percent higher energy density. However, self-discharge is 50 percent higher compared to NiCd, and discharge current is also limited [12].

The chemical reactions on the negative electrode are

$$MH + OH^{-} \rightleftharpoons M + H_2O + e^{-} \tag{2.4}$$

The chemical reactions on the positive electrode are

$$NiOOH + H_2O + e^{-} \rightleftharpoons Ni(OH)_2 + OH^{-} \tag{2.5}$$

The overall chemical reactions of Nickel-metal Hydride batteries are

$$MH + NiOOH \rightleftharpoons Ni(OH)_2 + M \tag{2.6}$$

Lead-acid was the first rechargeable battery invented by a French physicist. It has a cheap, simple manufacturing process but high self-discharge rate. In addition, Lead particles and toxic gases are released into the air during improper recycling operations.

The chemical reactions on the negative electrode are

$$Pb + SO_4^{2-} \rightleftharpoons PbSO_4 + 2e^{-2} \tag{2.7}$$

The chemical reactions on the positive electrode are

$$PbO_2 + 4H^+ + SO_4^{2-} + 2e^- \rightleftharpoons PbSO_4 + 2H_2O \tag{2.8}$$

The overall reaction of Lead-acid batteries is

$$Pb + PbO_2 + 2H_2SO_4 \rightleftharpoons 2PbSO_4 + 2H_2O \tag{2.9}$$

Therefore, among rechargeable batteries, Lithium-ion batteries have been widely employed by manufacturers because of their significant advantages, such as being relatively lightweight, long lifespan, high power, energy density, and low self-discharge rate [13].

In Table 1, key features of Nickel-cadmium, nickel-metal hybrid, lead-acid and Lithium-ion batteries are compared. The most important metric is the energy storage efficiency that is calculated by the Coulometric efficiency and energy efficiency [14]. Coulometric efficiency represents the ratio of the total charge extracted from the battery (discharge capacity) to the total

charge put into the battery (charge capacity) of a specific electrode [15]. Energy efficiency is the ratio of the amount of discharge power to the charge power in the cell.

Coulometric efficiency (CE) can be expressed as follows;

$$\begin{aligned} CE &= \frac{\int_{discharge} I\,dt}{\int_{charge} I\,dt} \\ &= \frac{\text{Total number of } Li^{+} \text{ ions back to cathode}}{\text{Total number of } Li^{+} \text{ ions departing from cathode}} \\ &= \frac{\text{Total number of } e^{-} \text{ back to cathode}}{\text{Total number of } e^{-} \text{ departing from cathode}} \end{aligned} \tag{2.10}$$

Energy efficiency can be expressed as follows;

$$\eta = \frac{\int_{discharge} IV\,dt}{\int_{charge} IV\,dt} \tag{2.11}$$

Figure 1 shows the relationship between specific energy and specific power. The secondary rechargeable batteries are evolving in two ways, reflecting increased specific energy for longer operating time and improved specific power for high current loads. A good balance is required, as improving one property may not strengthen the other. Specific power is the ability of a cell to deliver power in watts per kilogram (W/kg). Static energy is the capacity of a cell can store in watt-hours per kilogram (Wh/kg). Li-ion has better performance in terms of specific energy and specific output than Lead-acid, NiCd, and NiMH, which mean Lithium-ion battery has a longer cycle life and can meet high load requirements.

Table 1. Comparison of NiCd, NiMH, Lead-acid, and Li-ion batteries performance [14],[16],[17].

	NiCd	NiMH	Lead-acid	Li-ion
Commercial use since	1950	1990	1970	1991
Voltage (V)	1.2	1.35	1.93	2.4-4.1
Specific energy (Wh/kg)	35-80	55-110	30-40	100-300
Energy density (Wh/l)	50-70	160-420	50-90	125-600
Power density (W/kg)	100-150	100-500	100-200	500-5000
Maximum discharge rate	20 C	15 C	6-10 C	80 C
Energy efficiency	0.5-0.6	0.5-0.7	0.6-0.7	> 0.8
Cycle life (number of cycles)	300-1000	500-1000	200-400	> 2000
Self discharge (per month)	15-20	15-30	3-4	2-3
Operating temperature (°C)	-20 to 70	-20 to 65	-40 to 60	-30 to 70
Maintenance requirement	30-60 days	60-90 days	6 months	6 months
Cost (US$)	$50 (7.2V)	$60 (7.2V)	$25 (6V)	$100 (7.2V)

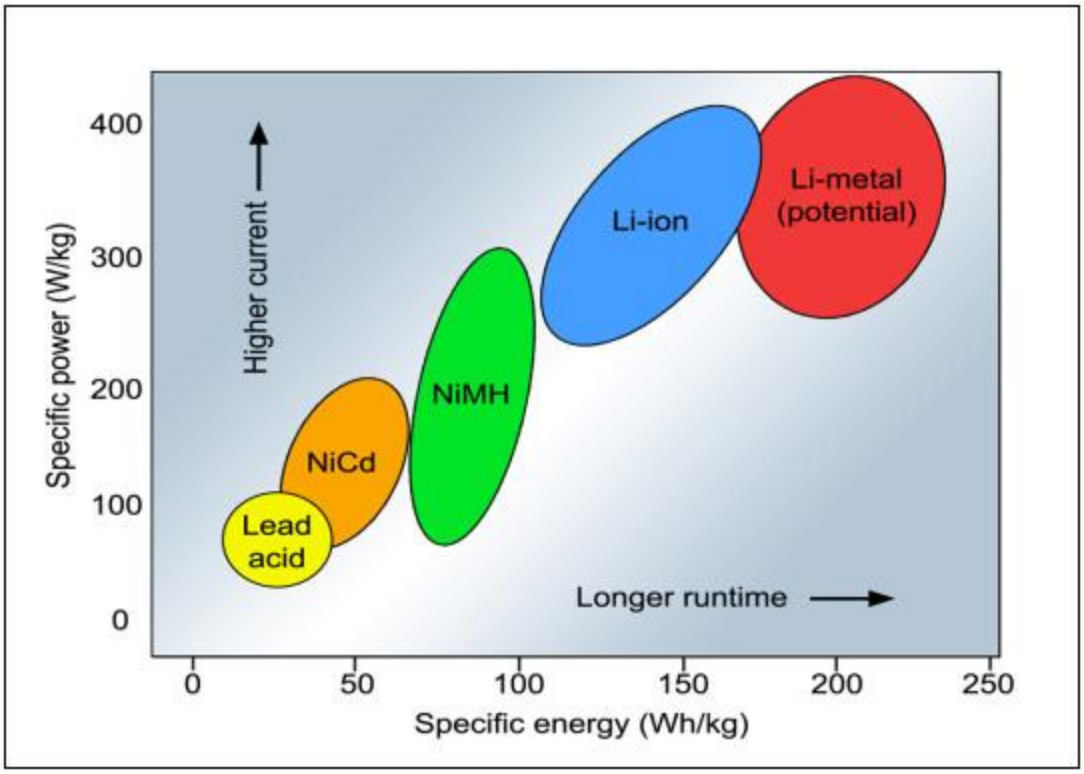

Figure 1. Specific power versus specific energy for rechargeable batteries: Lead-acid, NiCd, NiMH, Li-ion, and Li-metal [17].

2.2 Review of lithium-ion battery

2.2.1 Classification of lithium-ion batteries based on chemistry

Table 2 shows the commonly used chemistries of lithium-ion batteries. The positive electrode material may be different, while graphite is primarily used as the negative electrode material. Lithium cobalt oxide (LCO), used as the positive electrode material, has a relatively short life span, low thermal stability, and limited power capability. Since 1996, Lithium manganese oxide spinel (LMO) has been commercialized and used as the most common positive material.

LMO forms a three-dimensional spinel structure to reduce internal resistance and improve safety and thermal stability over LCO. The low internal resistance of the cell enables fast charging and a high current load for discharge; however, the life span is limited. Lithium nickel manganese cobalt oxide (NMC) is the most widely used positive material for Lithium-ion batteries. Nickel has a high specific energy and low internal resistance, and cobalt stabilizes the nickel. Combining the three substances properly improves the advantages of each other. Commonly known successful combinations are NMC532, NMC622, and NMC811. Nickel (Ni) increases the energy density while increasing the Manganese (Mn) content, reduce cell resistance [18]. However, high Ni content may cause severe capacity fade upon aging while high Mn content provides cycling stability [19].

Lithium iron phosphate (LFP) is another cathode material with high thermal stability up to 350^{o}C because the phosphate protects the material from deterioration at overcharge or high temperature. LFP is very safe material due to its stable olivine structure; it is non-toxic and inexpensive [20]. However, the drawback of LFP is low capacity, low energy density and high self-discharge rate. Also, it has relatively low equilibrium potential (3.4 V vs. Li/Li^{+}) and poor ionic conductivity, but its electrochemical performance can be improved by coating the particles with conductive carbon layer and by minimizing the particle size. Lithium nickel cobalt aluminum oxide (NCA) belongs to the cathode materials with layered structures like NMC, and $LiCoO_2$ has a high specific energy long life span of 200-260 kW/kg similar to NMC [21].

The most common anode material is graphite. It is abundant, safe, and has a high specific capacity. During charging and discharging, graphite is susceptible to volume change (about 10%) and mechanical stress. Mechanical stress can lead to crack propagation in the electrode leading loss of electrical conductivity and even total detachment. Also, more fresh surface is uncovered by the cracks and reacts with the electrolyte [22]–[24]. Such side reactions are facilitated by the high temperature induced by fast charging [25]. The process results in further growth of the SEI layer, which increases the resistance and causes both LAM and LLI. Due to the low potential of graphite (0.1 - 0.2 V vs. Li/Li^+), there is a high risk of lithium plating when cycling at higher currents and at cold temperatures.

Lithium titanate (LTO) has been used instead of graphite as the negative electrode material since the 1980s, and it forms a spinel 3D crystal structure. LTO has a relatively high equilibrium potential (1.55 V vs. Li/Li+) preventing SEI layer formation and the risk of lithium plating [26]. This enables the safe use of high charging currents and charging at cold temperatures. The LTO is capable of fast charging and can withstand a discharge current of up to 10C [27], [28]. Furthermore, LTO electrode has excellent cycle life and regarded as “zero-strain material” because it experiences almost no change in lattice dimensions upon lithium intercalation/deintercalation [29]. The main drawback of LTO electrode is low cell voltage and production cost is high.

Table 2. Comparison of commercial lithium-ion batteries [14], [16], [17].

	LCO	NCA	NMC	LMO	LFP	LTO
Name	Lithium cobalt oxide	Lithium nickel cobalt aluminium oxide	Lithium nickel manganese cobalt oxide	Lithium manganese spinel	Lithium iron phosphate	Lithium titanate
Positive electrode	$LiCoO_2$	$Li(Ni0,85Co_0,1Al_0,05)O_2$	$Li(Ni_0,33Mn_{0,}33Co_o33)O_2$	$LiMn_2O_4$	$LiFePO_4$	LMO, NCA, …
Negative electrode	Graphite	Graphite	Graphite	Graphite	Graphite	$Li_4Ti_5O_{12}$
Cell Voltage (V)	3.0-4.2	3.0-4.2	3.0-4.2	3.0-4.2	2.5-3.65	1.8-2.85
Energy density (Wh/kg)	150-200	200-260	150-220	100-150	90-120	50-80
Charge/discharge C-rate (C)	0.7-1/1	0.7-1/1	0.7-1/1-2	0.7-1/1	0.7-1/1-25	1/10
Cycle life (cycle)	500-1000	500	1000-2000	300-700	2000	3000-7000
Thermal runaway (°C)	150	150	210	250	270	250
Application	Electric devices	Medical devices, electric powertrain	E-bikes, medical devices, industrial	Power tools, electric powertrains	High load currents devices	Electric powertrain, UPS

2.2.2 Lithium-ion cell design

As shown in Figure 2, a battery can be categorized into the cylinder cell, button cell, prismatic cell, and pouch cell, dependent upon packaging. A cylindrical cell is one of the most common types used in lithium-ion or nickel-based batteries because of cost and safety. The manufacturing process of such cells is simple, so the production cost can be kept low. In addition, it has relatively good mechanical stability, which means it can withstand high internal pressure

without deformation and has a long lifespan. Moreover, most cylindrical cells have a pressure relief mechanism, such as a membrane seal, and find a wide range of applications. However, the disadvantage is the heavy weight and the low packing density due to the cavity space. The cylindrical cell is made of a jellyroll, current connectors, and safety devices. The Jellyroll design is used to manufacture the anode, cathode, and two separators into a hard, cylindrical can-shaped case. Jelly rolls are made by placing negative electrode separators, stacking separator sheets, a positive separator sheet, and another separator sheet rolled to form a cylindrical cell. The negative electrode is coated in copper foil, and the positive electrode is covered in aluminum foil. The thickness of the separator is usually around 20 micrometers. The current connectors are used to transmit electrons from batteries to devices. As shown in Figure 2, the cell consists of current connectors that include positive terminal, positive terminal lead, negative terminal, and negative terminal lead. Most of the positive terminal and negative terminal materials are stainless steel. Generally, aluminum alloys are used for positive terminal leads. Nickel alloy is typically used for the negative terminal [30]. Furthermore, safety devices are implemented into cylindrical cells to reduce the risk, such as a case, insulation plate, gasket, positive temperature coefficient (PTC) element, anti-explosive valve, and exhaust gas hole [31]. Common applications of cylindrical cells are in power tools, medical instruments, e-bikes, laptops, and electric vehicles [32].

Since 1995, a pouch cell has been used as a new design without metal housing [17]. By removing the metal housing, the weight becomes less, and the cell becomes the most space-efficient among different packaging types, being able to achieve 90-95% packaging efficiency. The pouch pack can be used in high-power or high-energy cells, reducing complexity by reducing the number of parallel connections inside the pack. The cells can be delaminated, and life can be extended by applying light stack pressure, and they are relatively stable.

On the other hand, the expansion that occurs during cell operation should be described. Expansion from incorrect placement can be up to 3% during operation, and the pressure generated can break the case. Therefore, the best ways are not to stack the cells on top of each other but to lay them flat side-by-side or leave some free space between them. Pouch-type lithium-ion cells can be further divided into two types, power and energy cells. The difference between the two cells is the ratio of active and passive materials in the cell. High-power batteries are designed to deliver high-current loads in a short period of time, which is used in HEV and high-load or force-generating power tools. Energy cells are designed to provide continuous energy over a long period and are suitable for use in EVs and scooters or e-bikes.

Prismatic cells were introduced in the 1990s to meet consumer demand for thinner cells. The cell can use the space optimally by using a layering method like the jelly roll of a cylinder cell. Because a hard shell, such as aluminum alloy or steel, is used, the structural strength is high, and the mechanical load-bearing capacity is good. On the other hand, the lifespan may be shorter

than cylinder-type cells and have poor thermal management efficiency, and, like pouch-type cells, they may also experience swelling. The prismatic cells have different applications depending on their capacity; cells in the 800mAh-4000mAh range are mainly used in mobile phones and tablets, while cells in the 20Ah-50mAh range are primarily used in EVs. Table 3 summarizes the characteristic of different battery types.

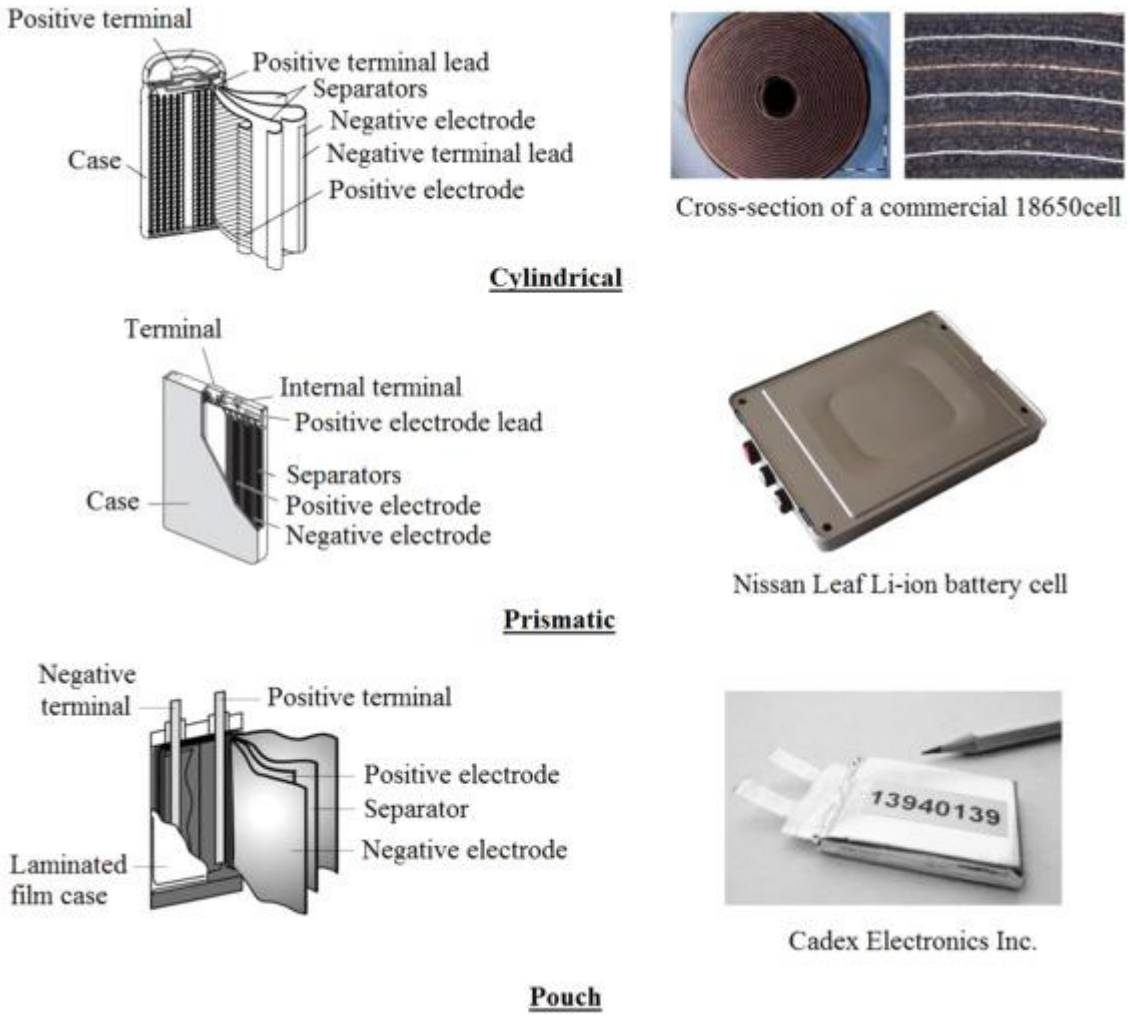

Figure 2. Schematic diagram of cylindrical, prismatic, and pouch cells [16].

Table 3. Review of different types of batteries.

	Cylindrical cell	Pouch cell	Prismatic cell
Energy density	Medium	High	High
Manufacturing cost	Low	Medium	High
Mechanical stability	High	low	Medium
Thermal performance	High	Medium	low
Pressure withstand	High	low	Medium
Volumetric efficiency	low	High	High

2.3 Working principle of lithium-ion battery

A Lithium-ion battery is composed of an anode (negative electrode), cathode (positive electrode), separator, electrolyte, and two current collectors. The electrodes are isolated from each other by a separator, which carries Lithium-ions through the electrolyte but blocks the flow of electrons. Figure 3 shows a schematic diagram of a Lithium-ion battery. The active material on the anode is typically made of graphite, while the active material on the cathode is commonly a lithium metal phosphate or a lithium metal oxide. Using a binder, the active electrode material has adhered to a current collector, typically aluminum foil on the cathode and copper foil on the anode [33]. The electrodes are immersed in an electrolyte containing solved lithium salt, and a separator is situated in the electrolyte between the electrodes.

The active material of the anode significantly affects electrochemical performances, such as the cyclability, charging rate, and energy density of cells. The active material of the cathode dictates the power and capacity of a cell.

During discharge, the battery provides an electric current and generates the movement of electrons from the anode to the cathode. Simultaneously, the anode releases lithium-ions to the cathode through electrolyte. When charging, the opposite reaction occurs. As described above, energy is stored electrochemically in a battery as chemical energy by the anode and cathode materials, which have different chemical potentials.

The half-reaction at the negative electrode is

$$Li_xC_6 \rightleftharpoons C_6 + xLi^+ + xe^- \tag{2.12}$$

The half-reaction at the positive electrode is

$$LiCoO_2 \rightleftharpoons Li_{1-x}CoO_2 + xLi^+ + xe^- \tag{2.13}$$

Combing equations (1) and (2), the full reaction is

$$LiC_6 + CoO_2 \rightleftharpoons C_6 + LiCoO_2 \tag{2.14}$$

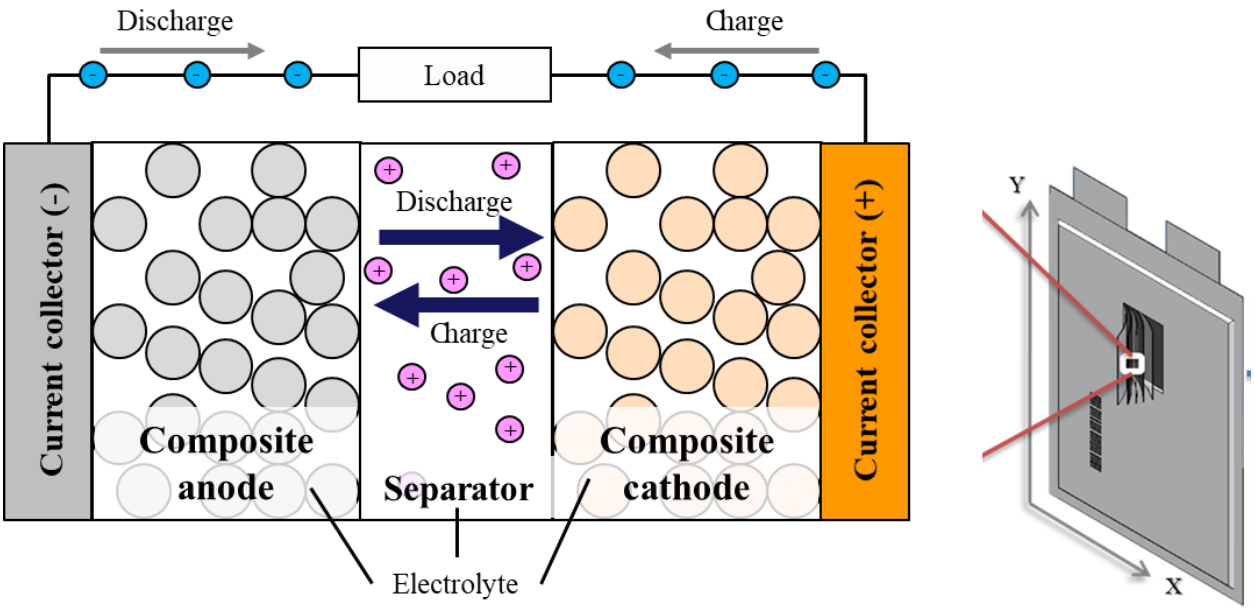

Figure 3. Schematic diagram of a micro cell during charge and discharge.

2.3.1 Cell voltage

The voltage of a cell is the potential difference between the positive and negative current collectors that are connected to the cathode and anode electrode. This is called the electromotive force, as the driving force that facilitates charges to flow [34].

$$V = U_p - U_n \tag{2.15}$$

where U_p is the potential at the positive current collector and U_n is the potential at the negative current collector.

2.3.2 Charge and discharge

Dynamic performance during charging and discharging is the speed at which current can be inserted and withdrawn from storage. During charging and discharging, the terminal voltages

increase and decrease, respectively. After charging or discharging is stopped, the terminal voltage response gradually recovers over time and reaches equilibrium. When the battery is overcharged, thermal runaway might occur because of a violent reaction between an overcharged cathode (deposited lithium) and an electrolyte solvent at a high temperature, resulting in a fast exothermic reaction between the delithiated cathode and the electrolyte.

The three typical ways to indicate the charge state of the battery at a certain point in time.

(1) State of Charge (SOC)

SOC is defined as the ratio of the remaining available capacity inside the battery to the maximum charge. The operating SOC range depends on the electrode materials. The SOC in percentage can be expressed as follows;

$$SOC(\%) = \frac{Q_{remaining}}{Q_{\max}} \times 100 \tag{2.16}$$

where Q_{max} is the maximum capacity of the battery.

Coulomb counting is one of the simple methods used to calculate the SOC in real time, where SOC is calculated by adding the integration of the current over time to the initial SOC. A fully charged battery is 100% SOC.

$$SOC(\%) = SOC_{initial} + \int_0^t \frac{I(\tau)}{Q_{nominal}} d\tau \times 100 \tag{2.17}$$

where $SOC_{initial}$ is initial SOC and $Q_{nominal}$ is the nominal capacity of a specific cell.

(2) State of health (SOH)

SOH is to estimate the maximum charge level of the battery compared to the initial value when the battery is first used. The ratio between the battery's maximum energy storage capacity at a given time and the maximum energy it was able to store initially is the formula for calculating SoH, which is expressed in percentage points.

$$SOH\left(\%\right)=\frac{Q_{\max}}{Q_{no\min al}}\times 100 \tag{2.18}$$

(3) Depth of discharge (DOD)

The DOD indicates the percentage of the battery discharged relative to the total battery capacity. This is one of the key parameters that can predict cell degradation. This is the opposite of SOC. When DOD is 0%, SOC is 100%, and when DOD is 100%, SOC is 0%. If the normal capacity was established sustainably, or if the actual cycling conditions and the normal operating conditions are different, the DOD may exceed 100% [14]. Figure 4 shows the measured voltages at different discharge C rates as DOD functions. The lower the C rate, the closer the battery is to 100% DOD. On the other hand, when C rate is high, the voltage drops quickly, indicating that only a portion of the capacity can be used.

Furthermore, DOD is an important parameter that directly affects cell degradation. When the battery is fully discharged, the battery SOH is reduced due to the potential volume change of the active particles increasing, and stress, cracks, and battery degradation may occur. Therefore, manufacturers specify the maximum recommended DOD for optimal performance [35], [36]. DOD in percentage can be expressed as follows;

$$DOD\left(\%\right)=\ 100\ -\ SOC\left(\%\right) \tag{2.19}$$

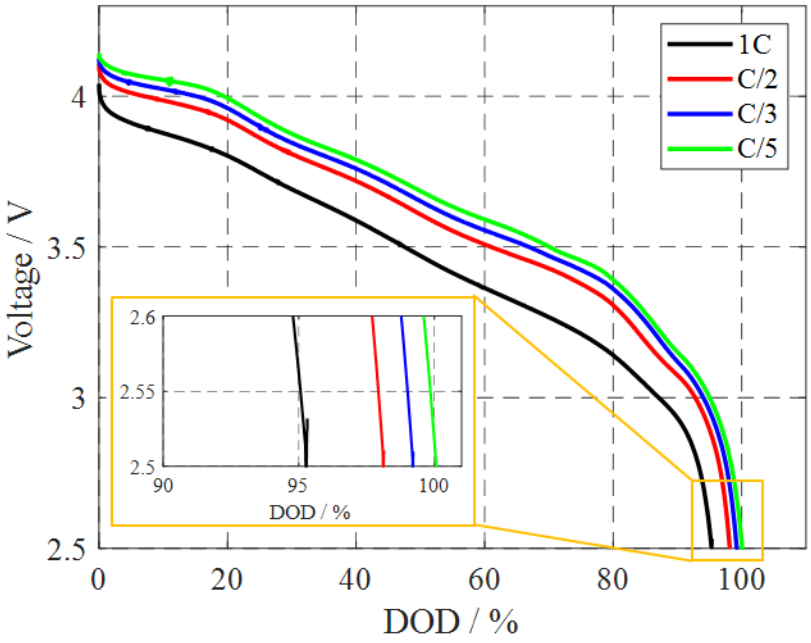

Figure 4. Voltage versus DOD for different discharge C rates (1C, C/2, C/3, and C/5) with partial zoom view.

2.3.3 Charging methods

The knowledge of various charging strategies helps to enhance cell life in the post-production phase. This helps to increase the life of the battery pack in a significantly shorter time [37]. The most typically used charging methods are as follows [38];

(1) Constant current (CC) charging

CC charging is a simple way to charge the cells using a constant current during the entire charging process and to stop the charge when a preset value of a terminal voltage is reached. The current charging rate significantly influences the battery performance. The challenging issue of CC charging is to set an appropriate charging current value that satisfies not only charging time but also capacity utilization. The high charging current provides a short charging time but severely

accelerates battery degradation. On the other hand, when the charging current is small, capacity utilization efficiency is high, but the charging time takes longer.

(2) Constant voltage (CV) charging

CV charging is a method of charging the battery with a constant voltage to prevent overcharging the cells. The battery life span is extended by avoiding overvoltage and irreversible side reactions. Voltage and current are related to the impedance of the cells. Accordingly, since the voltage is constant, the charging current gradually decreases as the cell is charged.

(3) Constant current constant voltage (CC-CV) charging

The CC-CV is a standard and by far the most common charging protocols for LiBs. It consists of a constant current charging phase where the battery voltage increases up to a cut-off value (CC phase), followed by a constant voltage hold until the current falls to near-zero (CV phase). Figure 5 shows an example of CC-CV charging profile for a large format pouch type lithium-ion battery. The CV phase allows for the concentration gradients within the electrode particles to disperse and is usually necessary to obtain high capacity utilization without exceeding the maximum voltage [10]. In contrast to CC-only charging, the charging time is substantially longer during the CV phase because the current steadily drop throughout this period. CC-CV is standard charging protocol in most applications due to its ease of implementation.

(4) Multi stage constant current (MCC) charging

Research have shown that shortening the charging time and limiting cell degradation may both be accomplished by adjusting the current levels while the battery is being charged. These

strategies are frequently driven by the need to generate less heat, to avoid situations that allow lithium plating, or to reduce mechanical stresses when the diffusion of Li^+ ions is restricted [39]. The MCC charging method includes several constant current steps, often followed by a CV stage. Since the anode potential is less likely to become negative at the start of the charging process, higher current values are typically selected for the earlier CC stages. When the terminal voltage reaches the predetermined limit, the current gradually decreases, and the charging continues until the cut-off current is reached [40],[41].

In order to overcome the problems of conventional charging methods, researchers have further proposed optimized charging methods using dynamic programming (DP) [42] and model predictive control (MPC) [43]. Table 4 summarizes the CC charging, CV charging, CC-CV charging, and MSS charging method, including advantages, disadvantages, and key parameters.

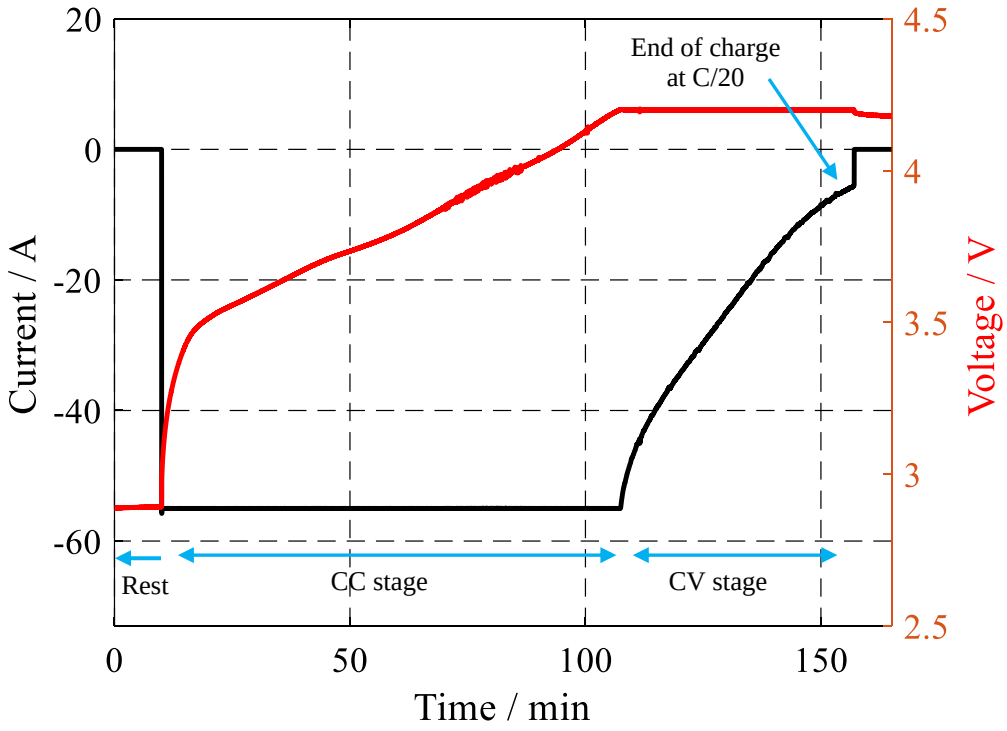

Figure 5. Constant current constant voltage (CC-CV) charging profile.

Table 4. Summary of advantages and disadvantages of charging methods.

Methods	CC charging	CV charging	CC-CV charging	MCC charging
Advantages	- Simple	- Simple	- High capacity utilization efficiency - Stable terminal voltage	- Simple - Fast charging
Disadvantages	- Low capacity utilization efficiency - Protective circuit required	- Causing the lattice collapse - Long charging time	- Charging speed - Energy loss - Temperature variation	- Charging speed - Capacity utilization efficiency -Battery lifespan
Key parameters	- Current rate	- Voltage limit	- Current rate in CC mode - Voltage limit in CV mode	- Optimal CC charging mode - Current rate

2.4 Temperature effect

In actual applications, the battery works at different ambient temperatures. The effects of temperature on batteries should consider three conditions, high, low, and gradient temperature.

At high temperatures, the lithium-ion battery degrades, corresponding to the almost positive electrode and electrolyte chemistries. Some degradation studies have shown that when a battery is repeatedly cycled while maintaining a high temperature, if the battery temperature rises above 50°C, the capacity and power fade can happen, even the discharge rate or cell chemistry [44],[45]. For example, the Sony 18650 cell suffered a 36% capacity fade after 800 cycles at 45°C and a more than 70% capacity fade at 55°C after 490 cycles [46]. In addition to performance degradation at high temperatures, the batteries are vulnerable to overheating due to a short circuit and excessive external temperature. If the thermal management system becomes out of control,

thermal runaway may occur with fire and explosion. Figure 6 shows a more detailed path progressing to thermal runaway according to the induced temperatures of various exothermic reactions [47]. SEI layer begins to be exothermic decomposition at temperature lower than 70°C. Once the layer is pierced, the negative electrode reacts with the electrolyte to generate combustion gas. As the temperature rises, the generally used positive electrode material will decompose and begin to produce oxygen. Oxygen and heat released during the reaction will cause batteries to fire and explosion [47],[48],[45].

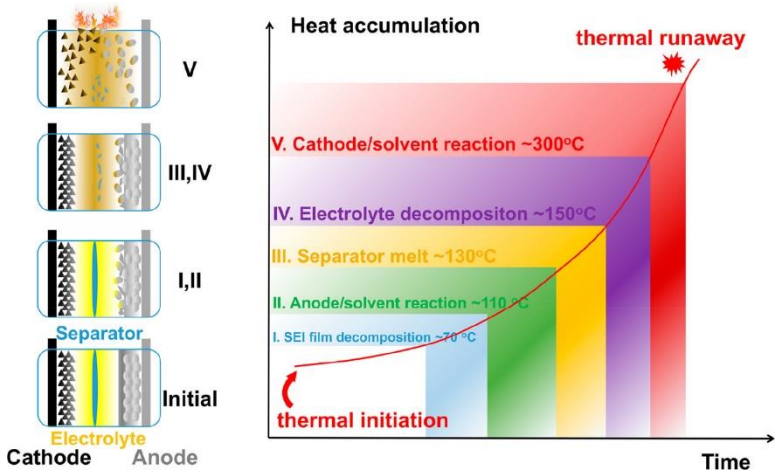

Figure 6. Schematic diagram of thermal runaway of lithium-ion battery [49].

At low temperatures, the battery performance is significantly reduced, and its use is limited. In general, a low temperature may affect a battery in various aspects, such as charging acceptance, energy and power capacity, and life span. Li-ion cell charged at a low temperature is difficult to charge with a capacity obtained at room temperature, and lithium plating may occur at a high charging speed [50], [51],[52]. At low temperatures of -40°C, only 1.25% and 5% of power and energy density could be transferred compared to the values obtained at 20°C. In addition to performance degradation, the aging of the battery is accelerated, especially at low temperatures below 0°C [53]. At low temperatures, the mechanism of poor performance is classified into several

aspects: (1) low ion conductivity of electrolyte; (2) limited solid state diffusivity of lithium-ion; (3) high polarization in the carbon anode; (4) high contact resistance between electrolyte and electrode interface. In an effort to improve performance at low temperatures, research is mainly focused on the development of new types of materials, including cathode, anode, solvent, and lithium salt for the electrolyte.

In addition, the uniform temperature distribution is one of the critical issues in ensuring that the battery operates efficiently. Non-uniform temperature distribution of cells, modules, or packs can result in different charging or discharging behavior and electrochemical performance. As the thermal and physical properties and geometrical parameters of the components are different, which means heat generation inside of the battery varies depending on the components, the heat transfer is different in all directions [54]. Therefore, a temperature gradient inside the cell may occur. In previous research, the temperature near the electrode was higher than elsewhere in the cell. As temperature increases, the electrochemical reaction rate exponentially increases according to the Arrhenius law [55]. Thus, non-uniform temperature distribution causes non-uniform chemical reactions of the electrode, which affects cell performance and lifespan [16]. For example, the method for examining the state change of the cell varies according to the temperature and non-uniformity of the battery pack level is proposed. As 5°C increases in temperature difference, the capacity loss of the pack may occur by 1.5-2%. In addition, efficient thermal control strategies in a challenging environment were proposed and showed that cells degrade about 10% capacity fade under a temperature difference of 5°C. In order to improve the performance of the battery, it is suggested that the temperature distribution between the cells and modules should not exceed 5°C [56].

As such, the lithium-ion battery is closely related to temperature, and it is crucial to understand how heat is generated and dissipated inside the battery.

2.5 Battery thermal management system (BTMS)

BTMS is responsible for managing and dissipating the heat generated during the electrochemical processes occurring in cells, allowing the battery to operate safely and efficiently. Its objective is to prevent accelerated battery degradation by managing the heat generated by its components so that it operates continuously under optimal temperature conditions.

The leading thermal management technologies that are commercially available or being researched by the scientific community are illustrated in Figure 7.

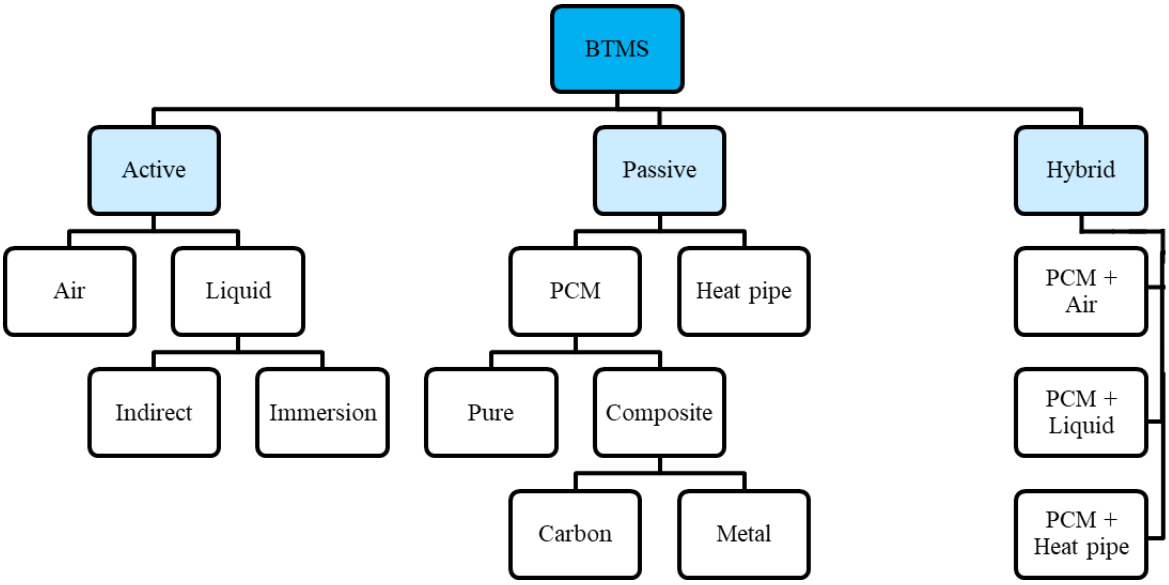

Figure 7. Leading BTMS technologies.

(1) Active BTMS

The most common active BTMS utilized in electric vehicles nowadays are those based on forced air or coolant. For instance, Toyota and Lexus use fans to blow cool air through the battery cells. Tesla, on the other hand, uses channels that are in direct contact with the cells and that allow a cooling fluid—typically a solution of water and ethylene glycol—to flow through them. When liquid coolants are utilized, they can either circulate inside pipes and act indirectly or be in direct contact with the cells. One of the main drawbacks of indirect systems in comparison to direct systems is the reduction in heat transfer efficiency, which is primarily due to the heat transfer resistance at the junction between the pipe carrying the refrigerant and the cell itself. Due to the low cost and the fact that there is no direct contact between the fluid and the electrical components of the battery, indirect cooling is the preferred alternative today by manufacturers who implement liquid cooling.

(2) Passive BTMS

Passive systems are an alternative to active BTMS that overcome their disadvantages. Among the various passive solutions, two method stands out: phase change materials (PCMs); and heat pipes (HPs). PCMs have been extensively studied for their application in BTMS. The interest of these materials lies in the possibility of exploring the high energies associated with phase changes that occur at a nearly constant temperature, making them very attractive when maintaining a homogeneous temperature throughout the battery-pack. In PCM cooling, the latent heat of the phase change of the cooling medium is used to absorb heat produced by the battery. Despite their good performance in achieving good thermal homogeneity in the battery pack, PCMs have a significant drawback that makes them not the preferred option today. These include the following:

limited thermal storage capacity and increased weight of the battery-pack. At high ambient temperatures, the PCM could melt completely without any heat being produced by the battery and the low thermal conductivity of the liquid PCM would then act as a barrier to heat transfer.

Heated pipes are a secondary substitute for active cooling systems. This technology involves the removal of heat by utilizing the liquid to vapor phase change and pressure gradients to ensure fluid motion. The heat pipe is composed of three sections: an evaporator, an adiabatic section through which the vapor circulates, and a condenser [10]. Although heated pipes are not currently used for battery pack cooling, they are widely used in the cooling of electronic components.

In general, the advantages and disadvantages of active and passive BTMS can be summarized in Table 5.

Table 5. Summary of advantages and disadvantages of active and passive BTMS.

	Active BTMS		Passive BTMS	
	Forced-air based	Based on coolant	PCM	Heat pipe
Advantages	- Simple design	- High efficiency	- Good thermal homogeneity	- low maintenance cost
Disadvantages	- High operating costs - Low efficiency	- Leakage problem - Occupied volume and complicity	- Low thermal conductivity - Limited thermal storage capacity	- Complexity - high manufacturing cost

(3) Hybrid BTMS

Hybrid systems, integrating two or more of the above choices, have been developed to take advantage of the benefits of active and passive systems. The use of PCMs with forced air, PCMs

with liquid cooling, or PCMs with heat pipes are the most researched hybrid system for pack cooling. The combination of PCMs with forced air help to achieve a good temperature distribution in the battery pack, while the combination of PCMs with heat pipes improves the heat transfer from the PCM to the outside of the cells so that the cells can be cooled by natural convection. Hmery et al. [57] coupled PCM with a liquid cooling system to enable the solidification of the melted PCM. The coupled system was shown to effectively cool a battery module during a 2C fast charge.

Although these BTMS systems show a much more effective performance than pure passive or active systems in thermally managing the battery pack, their complexity and cost are limiting factors for implementation in electric vehicles

2.6 Characterization of heat sources

2.6.1 Lumped thermal model

For a Lithium-ion cell with lumped thermal capacity, energy conservation balances heat generation, heat dissipation, and accumulation as follows;

$$\rho C_p \frac{dT}{dt} = \dot{Q}_{gen} - \dot{Q}_{loss} \tag{2.20}$$

where ρ is the bulk cell density, C_p is the bulk specific heat capacity, $\dot{Q}_{gen}$ is the heat generation rate in the battery and $\dot{Q}_{loss}$ the heat exchanged with the surrounding environment, which is given by the convection heat transfer term. The convection heat transfer term can be expressed through Newton's low as follows;

$$\dot{Q}_c = h A \left(T - T_{amb} \right) \tag{2.21}$$

where h is the convection transfer coefficient, A is the thermal area, and T_{amb} is the ambient temperature.

2.6.2 Simplified heat generation

The thermal behavior of a lithium-ion battery can be strongly affected by the electrochemical and chemical processes involved in charge and discharge. Heat generation is a complex process that requires an understanding of how electrochemical reaction rates vary with time and temperature and how current is distributed. The heat generation can be grouped as irreversible and reversible heat as follows;

$$\dot{Q}_{gen} = \dot{Q}_{irreversible} + \dot{Q}_{reversible} \tag{2.22}$$

The irreversible one represents Joule heating induced by overpotentials, that is the difference between open-circuit voltage (OCV) and cell terminal voltage, indicates Ohmic, charge-transfer overpotentials, and mass transfer limitation. The reversible one is related to changes in OCV with respect to temperature and SOC.

Bernardi et al. [58] formulated the thermodynamic energy balance for a single cell and derived a simplified heat generation form under the assumption that no heat from phase changes or heat from mixing, uniform temperature or SOC, and only one electrochemical reaction takes

place. The heat from mixing can usually be neglected for the electrochemical system with good transport properties [59]. The total heat generation rate can be expressed as follows;

$$\dot{Q}_{gen} = I\left(U_{OC} - V\right) - I \cdot T \cdot \frac{dU_{OC}}{dT} \tag{2.23}$$

where U_{OC} is the open circuit voltage, V is the terminal voltage, and I is the charge and discharge current that is defined as positive when the battery is discharged.

The reversible heat generation rate can be expressed as follows;

$$\dot{Q}_{rev} = I \cdot T \cdot \frac{dU_{OC}}{dT} \tag{2.24}$$

where $\frac{dU_{OC}}{dT}$ is the entropy coefficient that is a function of SOC.

According to the Gibbs free energy change, the entropy change of the cell reaction can be related to the open circuit voltage. The Gibbs free energy change is given by

$$\Delta G = \Delta H - T\Delta S \tag{2.25}$$

where ΔG is Gibbs free energy change, ΔH is enthalpy change, and ΔS the entropy change. The Gibbs free energy can be also be described as follows;

$$\Delta G = -nF\left(U_{OC}\right) \tag{2.26}$$

where F is the Faraday constant, and n is the stoichiometric number of electrons participating in the reaction of the cell (n=1 for a lithium-ion battery). By combining equations (2.25) and (2.26),it is seen that the open circuit voltage is composed of enthalpy and entropy change terms and can be written as follows;

$$U_{OC} = -\frac{\Delta H}{F} + \frac{T\Delta S}{F} \tag{2.27}$$

Equation (2.27) can be used to determine the enthalpy and entropy change value from the cell open circuit voltage at different temperatures. The entropy coefficient consists of the entropy change term.

$$\frac{dU_{OC}}{dT} = \frac{\Delta S}{nF} \tag{2.28}$$

The entropy coefficient can be either positive or negative depending on the charging or discharging of the battery.

On the other hand, the irreversible heat generation rate can be calculated as follows;

$$\dot{Q}_{irr} = I\left(U_{OC} - V\right) \tag{2.29}$$

It can be o be expressed as follows;

$$\dot{Q}_{irr} = I^2 R \tag{2.30}$$

where R is the internal resistance.

3. Design of test station

3.1 Experiment setups

In order to measure the HGR of lithium-ion batteries, a test station is designed and constructed to create operating conditions suitable for the purpose with stability and accuracy. The characteristics of the battery can be assessed with the collected data by the test station. The test station has the following design criteria;

- Charge and discharge the battery with different profiles such as driving cycle, CC-CV charging, CC discharging, HPPC, and pulse charging.
- Protect overcharge and discharge using an extra programmable logic controller (PLC).
- Measure terminal voltage, current, temperature, HGR, pressure, thickness change, and impedance.

3.1.1 Specification of test station

Figure 8 shows a schematic diagram of the experimental setup of the test station. The hardware is categorized into experimental equipment and testing instrument. For experimental equipment, the thermal chamber provides a stable ambient temperature. The power supply is used to supply electric energy to the battery under constant voltage and constant current mode. The electronic load is used to consume the electric power of the battery under constant current, constant resistance and constant power mode. The battery protector is composed of two relays and a

programmable logic controller. Testing instruments are categorized into sensors and data acquisition (DAQ) systems. Sensors are used to measure parameters: voltage, current, temperature, HGR, and pressure. The terminal voltage is measured through the battery tab directly. Current is measured through a current transducer which converts current into a voltage signal that connects the analog input of the DAQ board. Thermocouples measure the surface temperature of the cell and ambient temperature and are connected to the temperature modules of the DAQ board. Heat flux sensor measures the flow of heat during charging or discharging and produces proportional output voltage. The collected output voltage is converted into HGR by multiplying the calibration coefficient obtained by the calibration. The pressure sensor measures the pressure applied to the cell placed into the calorimeter and monitors the volume change during charge or discharge.

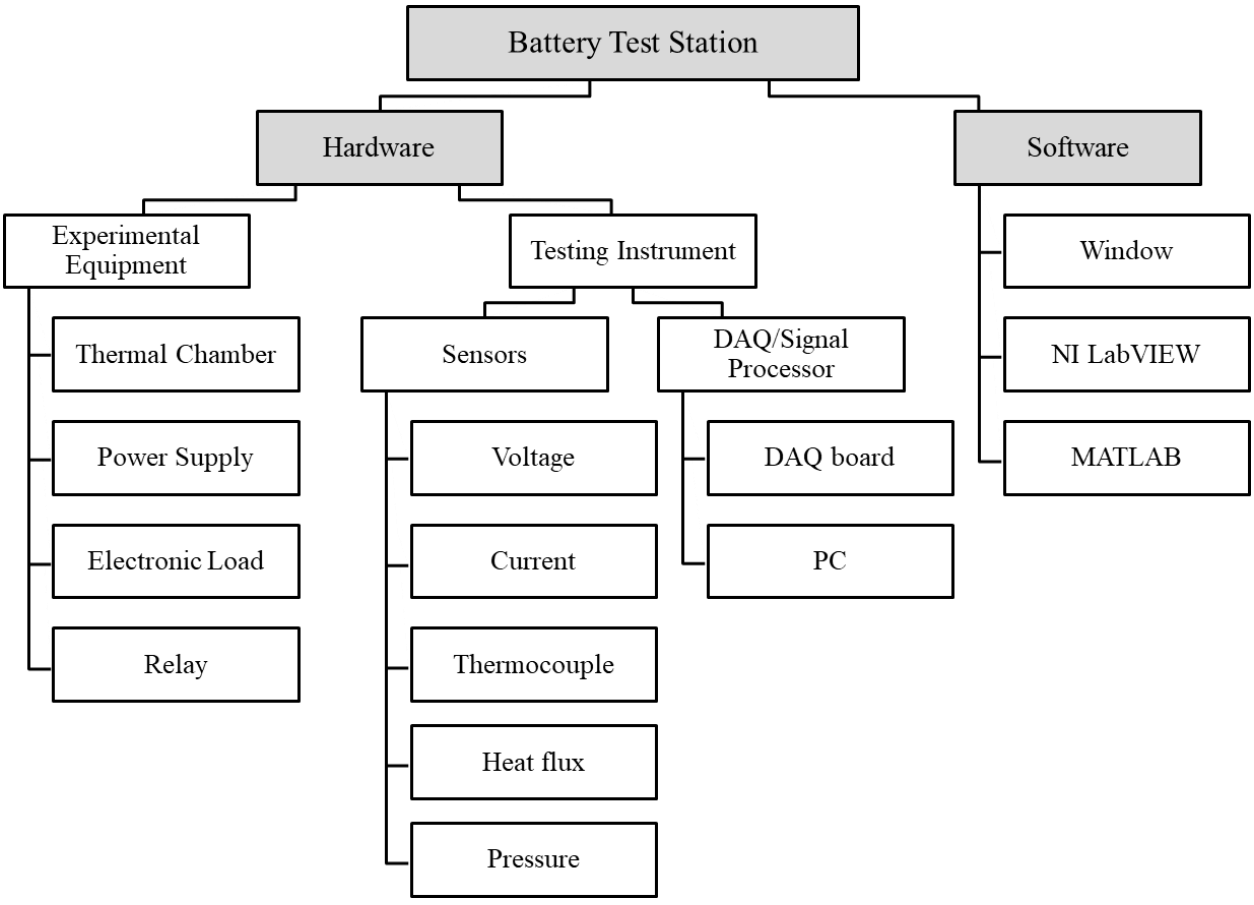

Figure 8. Schematic diagram of the test station.

The overall software structure is shown in Figure 9. The software mainly uses LabVIEW of National Instrument. PC is used to control and monitor equipment via LabVIEW, which creates an easy-to-use user interface code. LabVIEW can start or stop testing, switch charge or discharge modes, create appropriate outputs using analog signals, and initialize equipment. Data can be read, monitored, and collected via DAQmx system associated with LabVIEW. It uses four types: analog input, output, temperature, and digital.

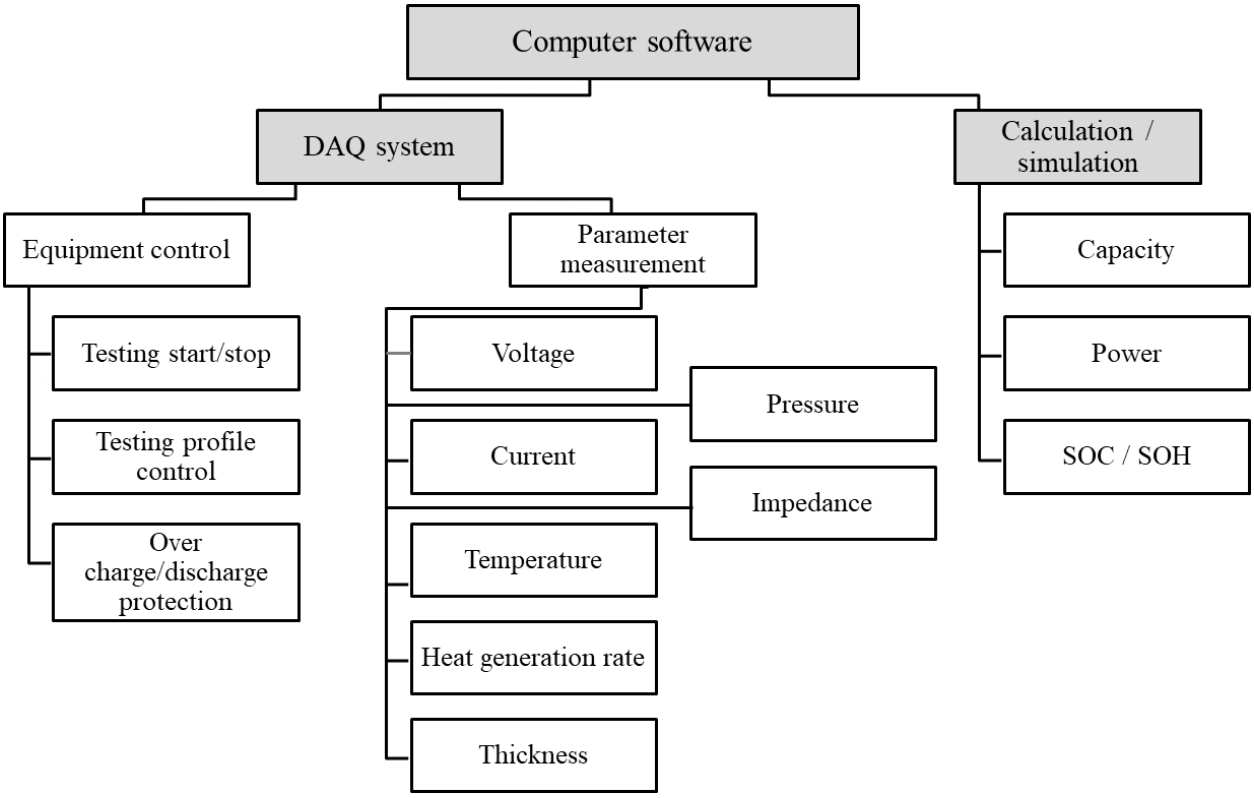

Figure 9. Schematic diagram of computer software system.

The overview of battery hardware is shown in Figure 10. When a battery is placed into the holder, then terminals are connected to the output of the power supply for charging and electronic load input for discharging. The power supply and E-load are controlled via analog outputs signals given by the LabVIEW. In addition, prevention for overcharging and discharging of the battery is implemented using a PLC and two relays that controls the connection of the power supply and electronic load, respectively. The PLC monitors the voltage in real time and disconnects the circuit when the limits are exceeded.

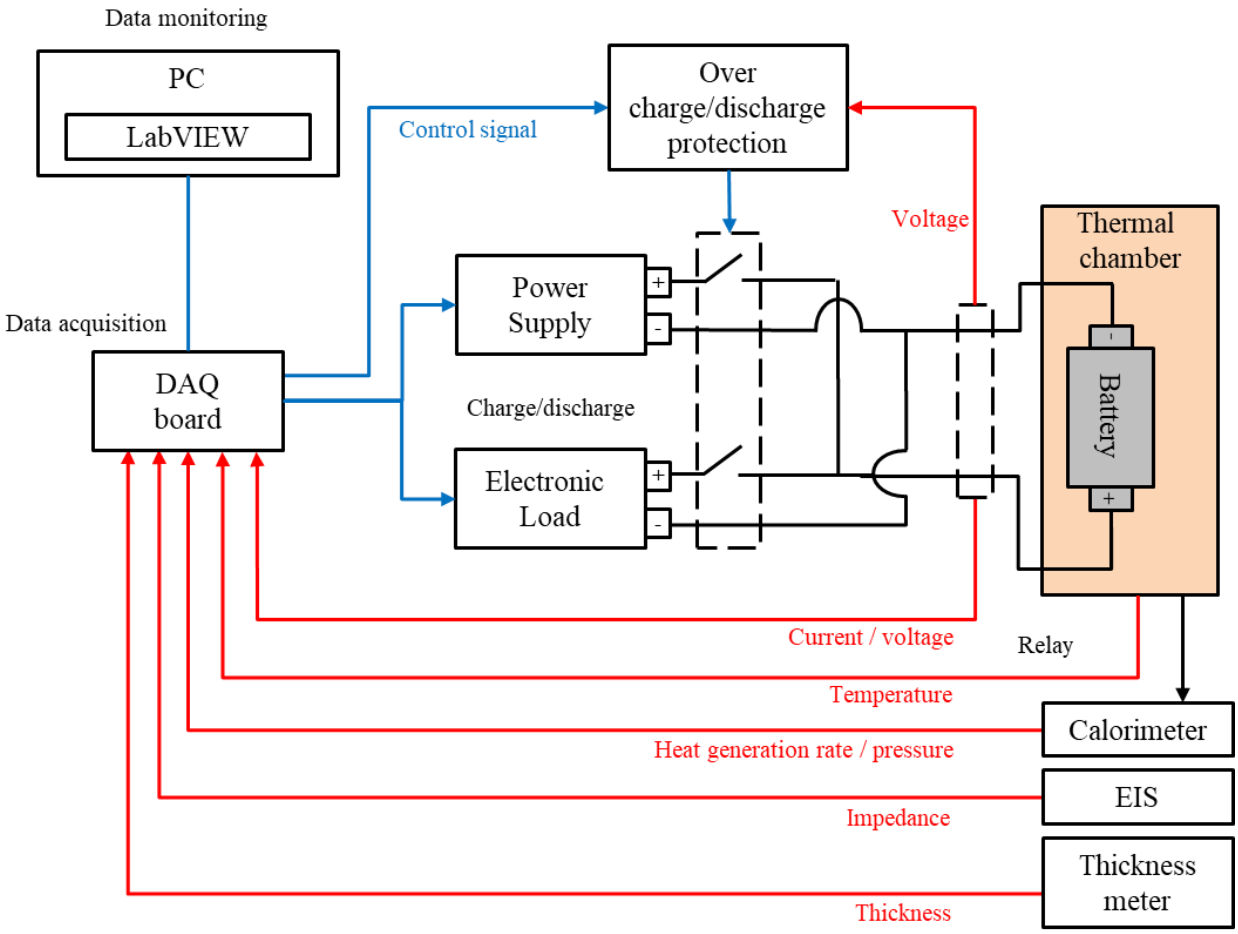

Figure 10. Schematic diagram of the battery hardware.

3.1.2 Design of calorimeter

A calorimeter is designed to measure the HGR of a cell during the charge and discharge cycle. Figure 11 (a) shows a side view of the calorimeter. The calorimeter designed for the pouch type of a cell has a sandwich structure, where the cell is placed between two Direct-to-Air-TEAs. A thermal paste and sheet are used to increase thermal conductivities between the cell and the TEA. TEA can directly and bidirectionally transfer the heat generated and works as a heat pump. The TEA includes a fan and several TEMs, foam, and heat sinks, as shown in Figure 11. Fans are used

to promote the transfer of the generated heat to the ambient. The free space between the components is filled with foams for insulation, so all of heat should transfer through TEA, which maximizes the cooling or heating efficiency of the calorimeter. The metal plate is the hot side as the heat is pumped by the TEMs, and the fan is the cold side as it transfers heat to the surrounding environment.

The metal plate is shown in Figure 11 (b)-(c), where six holes are tapped for the springs and bolts used for applying pressure. The TEMs have constructed semiconductor devices based on Peltier effects that transfer heat from one side to the other or vice versus, depending on the direction of the input current, heating or cooling the cell. The metal plate is responsible for efficiently conducting heat between the TEMs and the cell.

The power needed for TEA is supplied by a bipolar power supply. In order to control the surface temperature, three K-type thermocouples are attached on the lower TEA, one on the positive side, one on the middle, and one on the negative side. In order to set the initial pressure condition, two pressure sensors are placed, one to the positive and the other to the negative. Three heat flux sensors are placed on the upper TEA, one to positive, one to negative, and one to the center generating an output voltage proportional to the heat flow between the cell surface and the metal plate during charging and discharging. The output voltage signal is recorded as a function of time via DAQmx system and is used to calculate the HGR.

Additionally, since the cell is in close contact with the TEAs, it becomes an isothermal system without considering the heat capacity of the cell. The specifications of a TEA are summarized in Table 6.

Table 6. Specification of TEAs.

Specification of TEA	
Dimension (mm)	545 × 120
Control voltage (V) / current (A)	24 / 18
Maximum heat pump rate per section (W)	300
Fan voltage (V)	100
Weight (kg)	8.9

(a)

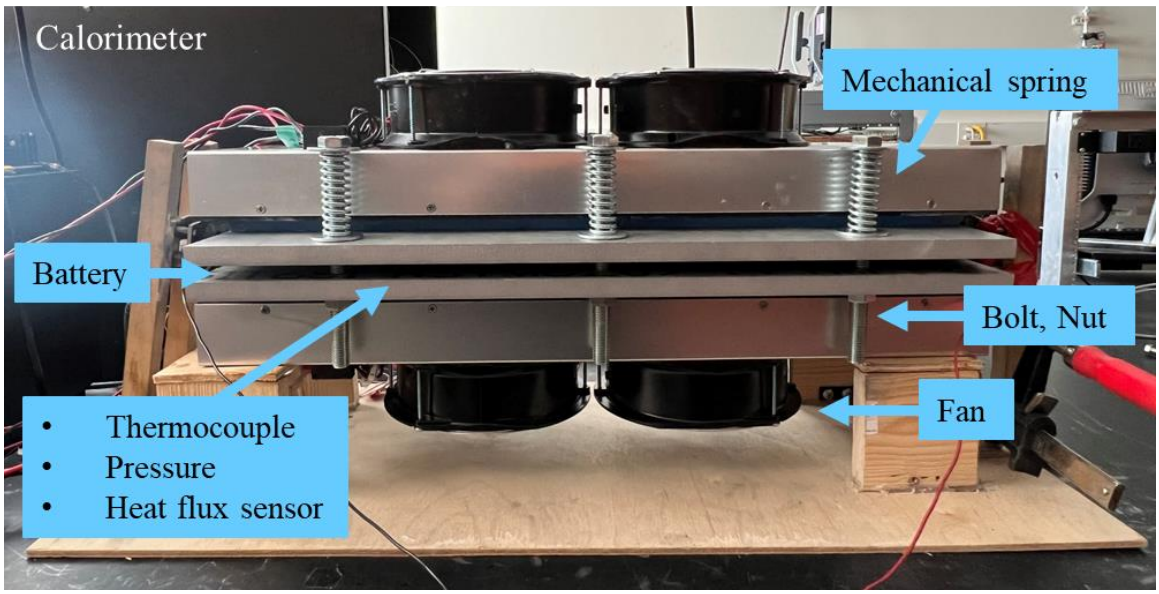

(b)

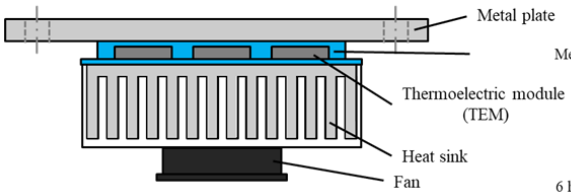

(c)

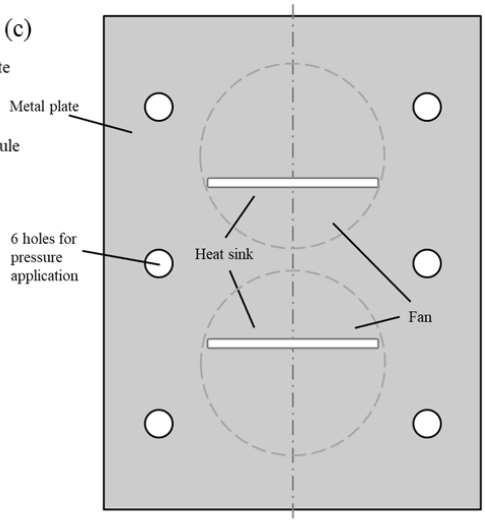

(d)

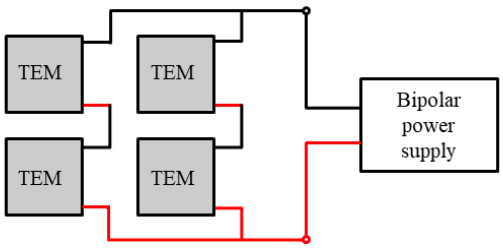

Figure 11. Conceptual drawing of a calorimeter: (a) overview of the calorimeter, (b) side view of a TEA, (c) top view of a TEA, (d) connection of 4 TEMs in TEAs.

After construction of the calorimeter, sensors should be calibrated. First, thermocouples are calibrated using ice point calibrators. After setting the desired temperature in the calibrator, and the temperature is set, the thermocouple is connected to the probe and the temperature are read by computer. If the measured temperature is different from that by the ice point calibrator, the difference is compensated using the controller. In addition, the pressure sensor is used to set a reference pressure or to monitor the pressure in real time during charging and discharging. The sensing system was also calibrated by reading the voltage signal corresponding to the weight using a standard weight.

Moreover, the heat flux (HF) sensor should be calibrated to calculate the generation rate [6],[60]. Three heat flux sensors are located on the negative electrode side and the center and positive electrode side. All sensors used for the three segments are the same, but the performance of each can be different. Firstly, three thin-film flexible polymer heaters with the exact dimensions are attached as the heat flux sensor to each segment and set the desired temperature with a calorimeter. 30 minutes long is rested to stabilize the temperature. Then, the current is increased to the heater in a step by a controlled digital power supply. Each step took 10 minutes long and was repeated up to 50W, while the calorimeter should maintain the set reference temperature.

The calibration was carried out in the same procedure in the uniform temperature case and non-uniform temperature case. The calibration result at a uniform temperature, which keeps the temperature of the three segments the same as 25°C, is plotted in Figure 12 (a)-(c). As shown in Figure 12 (a), the temperatures of the three segments are maintained at 25°C during the calibration. When the power input for the heat increases with a step of 10W powered by a bipolar supply, there

is an overshoot of around 0.1°C in the temperature control loop. Figure 12 (b) shows the voltage output of the three heat flux sensors from 0 to 50W. Figure 12 (c) shows the relationship between the output voltage versus HGR. After an adjustment for 0W, the measured heat is plotted as a function of the voltage outputs using the polymer regression method.

For the non-uniform temperature, the temperature at the positive and negative electrode side at 28.33°C and the center at 18.33 °C is set respectively, which average is 25°C. The calibration results are plotted in Figure 12 (d)-(f).

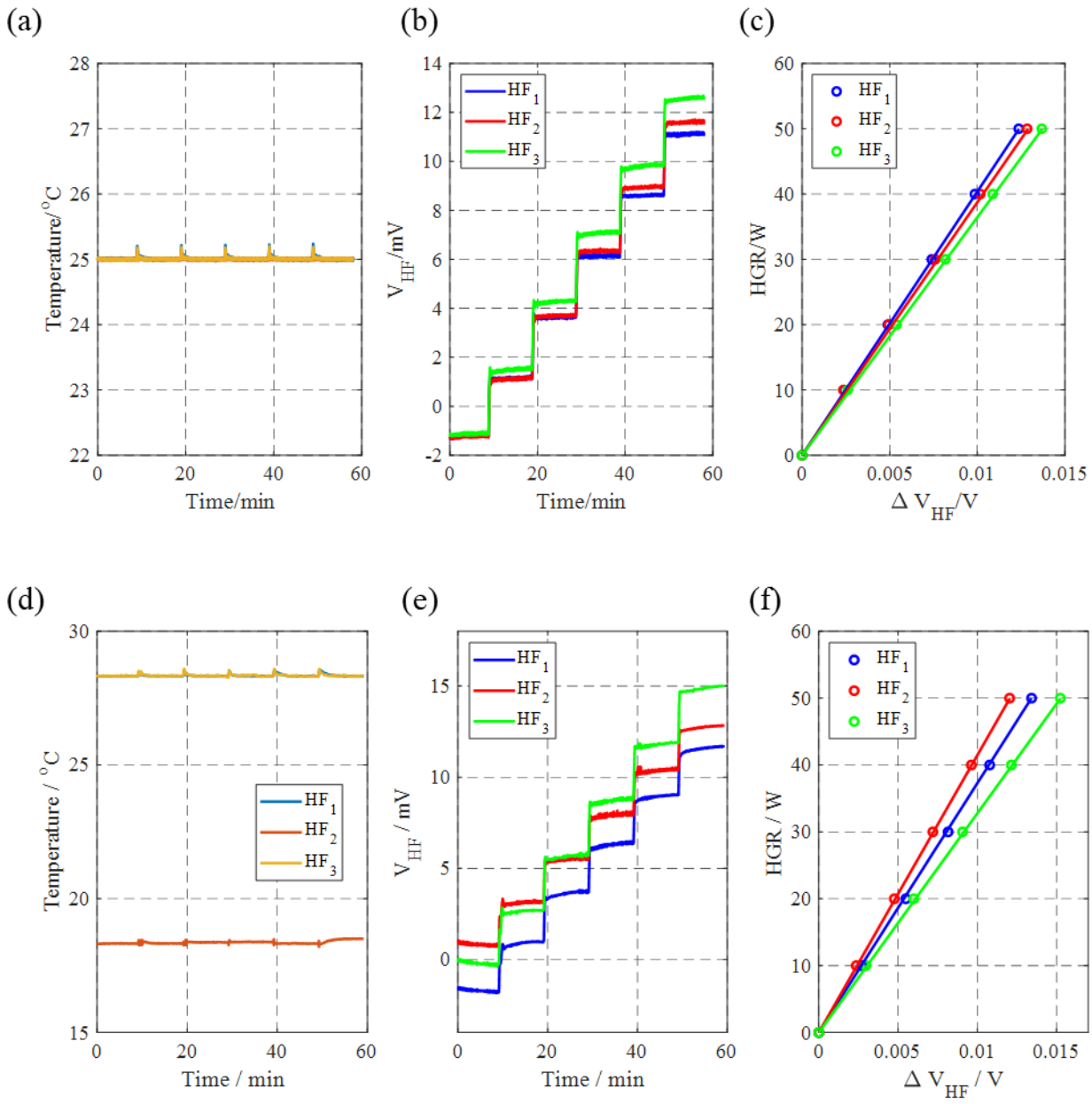

Figure 12. Calibration results of the three heat flux sensors: at uniform temperature, (a) average surface temperature, (b) output voltage data of the heat flux sensors, (c) HGR versus the output voltage data of the heat flux sensors; at non-uniform temperature, (d) average surface temperature, (e) output voltage data of the heat flux sensors, (f) HGR versus the output voltage data of the heat flux sensors.

Table 7 shows the linear equation with parameters for each heat flux sensor used for uniform and non-uniform temperature distributions. Even with the same sensors, the output of the sensors are different. Thus, the parameters becomes different, which should be compensated by the obtained equations.

Table 7. Calibration result of heat flux sensors at uniform temperature and non-uniform temperature.

Equation: $y = a \cdot x + b$	Uniform temperature : 25(-)/25/25(+)°C		Non-uniform temperature : 28.33(-)/18.33/28.33(+)°C	
	a	b	a	b
Heat Flux 1 (negative)	4037.2	5.3354	3726.3	6.3404
Heat Flux 2 (center)	3873.7	5.4701	4145.0	-3.0380
Heat Flux 3 (positive)	3644.5	4.5702	3276.1	1.0823

Figure 13 shows a picture of the overall test equipment used for the experiment. Figure 13 (a), (b) and (c) show the thermal chamber, test station, and a large format pouch type lithium-ion battery. As shown as Figure 13 (b), PC, power supply, electronic load, and cell protectors are well organized in the rack.

Figure 13. Experiment setup: (a) thermal chamber, (b) overview of a multifunctional test station, (c) a large format pouch type lithium-ion battery.

3.2 Cell characterization test profile

3.2.1 Specification of cell

The cell used for the experiment is a large format pouch type Lithium-ion battery with NMCA/graphite-SiO_x chemistry. The specification of the cell is as follows;

- Active materials: NMCA for cathode and graphite and SiO_x for anode
- Nominal capacity: 110Ah
- Nominal voltage: 3.63V
- End-of- charge voltage, current: 4.2V
- End-of-discharge voltage: 2.5V, 5.45A
- Dimension: 580mm (L)*112.4mm (W)*9.0mm (T)

3.2.2 Experimental measurements

(1) Open circuit voltage (OCV)

The open circuit voltage of battery is the voltage when no load is connected to the battery. OCV vs SOC is the important data that represents the characterization of the cell performances. OCV is measured by the voltage relaxation method as a function of SOC and temperature. A cell is fully discharged and charged with at low current C rates, where the terminal voltage is measured at equivalent SOC intervals after a sufficient relaxation time. In this experiments, the data were collected at a sampling time of 0.1 second. OCV is determined as the average terminal voltage measured during charging and discharging.

Figure 14(a) shows the measured terminal voltage (red line) and current profile (black line) for OCV measurement. First, the cell was placed into the thermal chamber to maintain a constant ambient temperature of 25°C and rest for 10 hours. Then, the cell is fully charged with 0.1C CC-CV mode and then discharged with 1% SOC intervals at 0.1C CC mode. The measurement time for a 1% SOC decrease was calculated using the capacity that was measured with the C/3 CC-CV charge and C/3 discharge profile. At the end of the discharge, the cell is rested for an hour to reach equilibrium state. This process is repeated 21 times until the cell reaches the discharge cut-off voltage. The partial zoom view of the measured terminal voltage and current is shown in Figure 14 (b). The profile of partial zoom views includes is the measured terminal voltage and current while the battery is fully charged at 0.1C CC-CV and discharged as much as 2% SOC. For CV mode, the cut-off current is set to C/20 (5.45A). When the cell reaches 4.2V, the charging mode switches from CC to CV mode, and the current is decreased until reaching cut-off current while the voltage is maintained as 4.2V. After the cell is fully charged, the voltage stabilized to a certain point within 1 hour because the cell is charged with a small current. Then, the battery is discharged at C/10 CC mode for 360 seconds that is the discharge time by 1% SOC decrease.

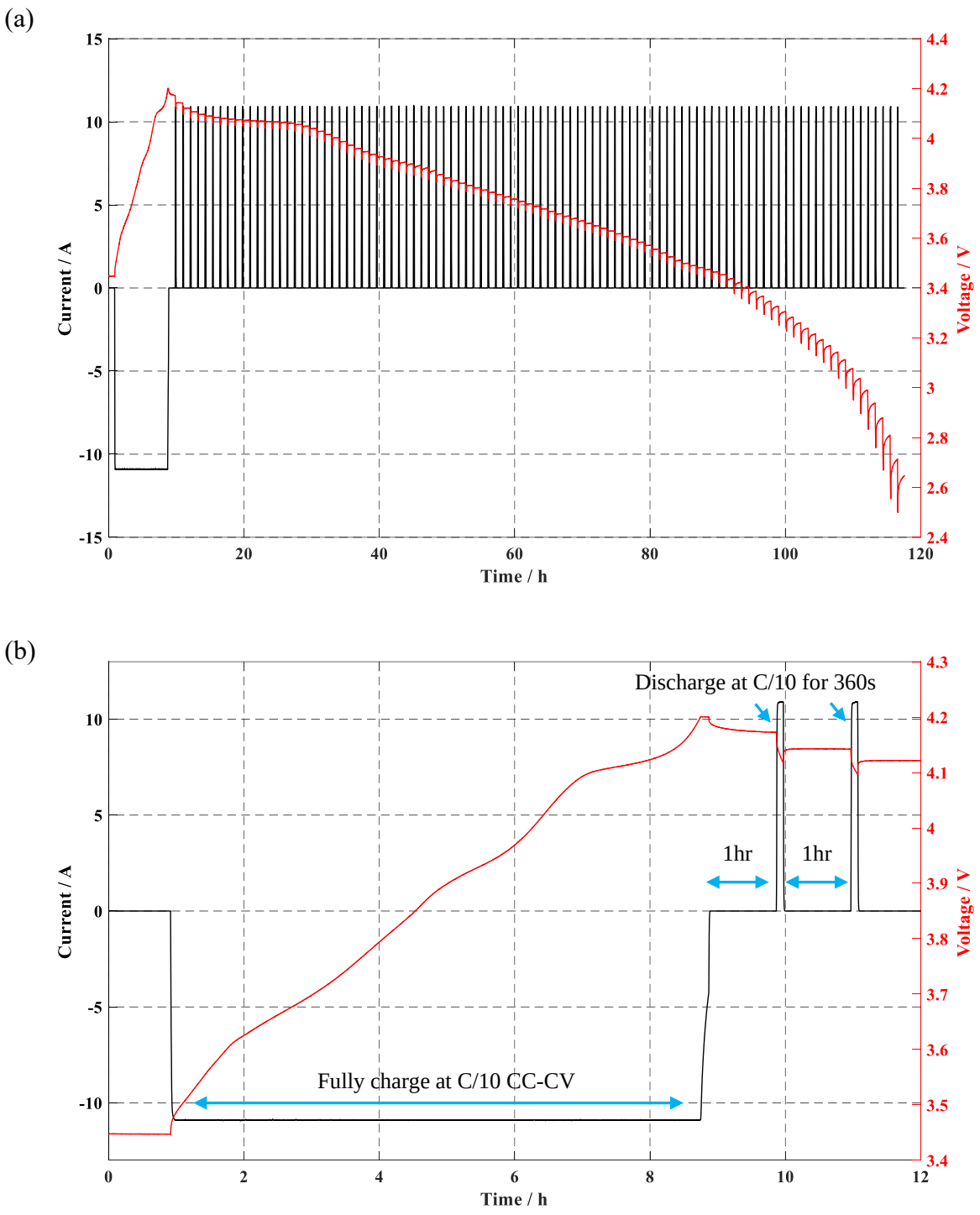

Figure 14. OCV measurement profile during discharging at 25°C: (a) terminal voltage and current, (b) partial zoom view of terminal voltage and current.

The measured OCV by charging and discharging and the average of the two values are plotted in Figure 15. The discharge OCV is less than the charge OCV. Depending on the characteristics of the battery materials, the equilibrium potential of the battery differs each other when charging and discharging under the same SOC points. This phenomenon is known as battery hysteresis [41],[42],[63]. Previous studies have indicated the causes of hysteresis by thermodynamic entropy changes and mechanical stress in active material particles [64],[65],[66]. Konishi et al. proposed that the large potential hysteresis between charge and discharge processes in Li1.2Ni0.13Mn0.54Co0.13O2 is primarily related to the reaction that is compensated with oxygen redox [67]. The hysteresis of the LiFePO4 battery is demonstrated experimentally as a thermodynamic effect caused by strain accommodation energy [68]. Lu et al. [69] analyzed effects of the particle size of active materials. As the ionic radius decrease, the hysteresis voltage decrease. The authors analyzed the dependence of hysteresis phenomena on major variables such as temperature, current rate, SOC, and ion path during charging and discharging. Experiments showed that as SOC decrease, the hysteresis effect increases, and minor loop hysteresis is limited by major hysteresis [70]. Therefore, an average value of charge and discharge OCV is calculated and used for the thermal model to predict the generated heat of the battery.

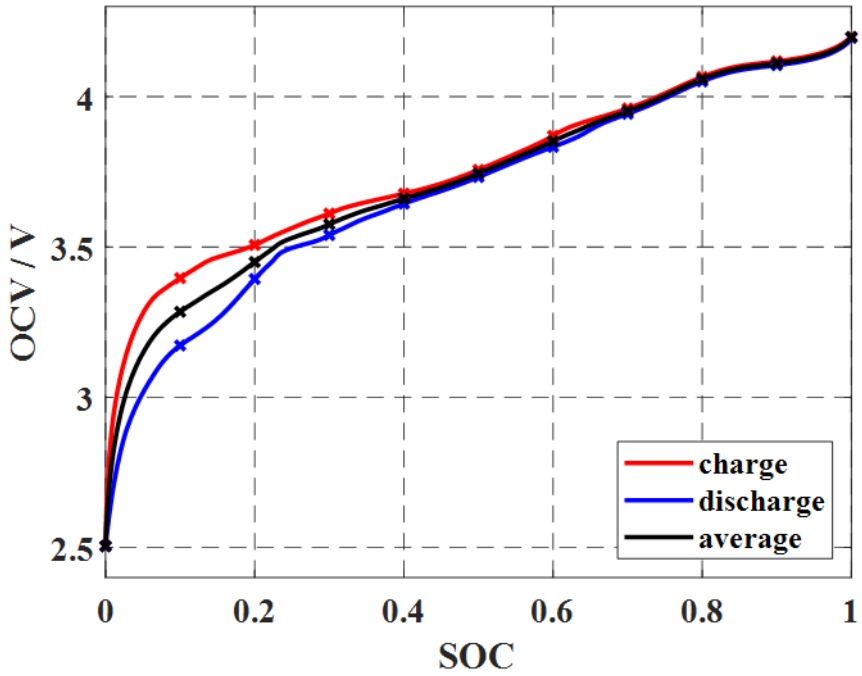

Figure 15. OCV – SOC curve in charge, discharge, and average between charge and discharge.

(3) Hybrid pulse power characterization (HPPC) test

The HPPC is used to determine the dynamic performance of the battery over usable voltage ranges such as the power capability of the cell. A testing profile, including regeneration and discharge pulses under different SOCs, is used at different temperatures and current loads.

The current and voltage profile of the HPPC test is plotted in Figure 16 (a) based on the battery test manual for electric vehicles recommended by the U.S. department of energy [71]. The partial zoom view of the measured terminal voltage and current is shown in Figure 16 (b). First, the cell is sufficiently rested in a thermal chamber at 25°C and then fully charged with C/3 CC-CV mode. The cut-off current of CV mode is C/20 (5.45A) that is the same as that in OCV measurement. After resting for an hour, the fully charged cell is discharged at a 1C CC pulse for 30 seconds, and after resting for 60 seconds, the cell is charged at 1C CC pulse for 30 seconds. Following a rest period, the cell is immediately discharged at C/3 CC for 577 seconds that is

operation time as 5 % decreases. The discharging time was established by capacity at beginning of life. This sequence is repeated for every 5% SOC points until the cell reaches to cut-off voltage.

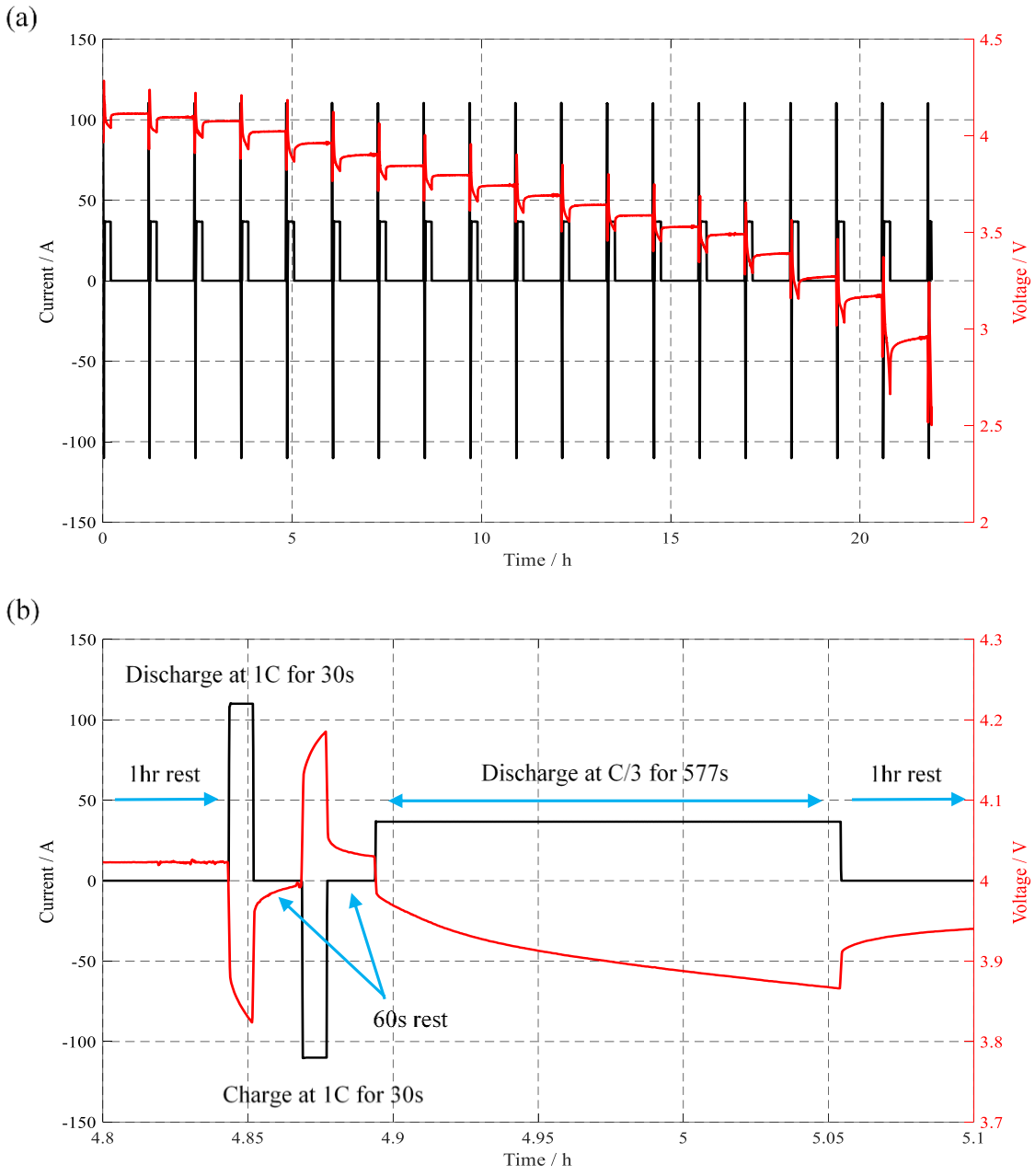

Figure 16. HPPC test profile at 25°C: (a) terminal voltage and current, (b) partial zoom view of terminal voltage and current.

The resistance of regeneration and discharge by the HPPC test at different SOC is shown in Figure 17. The range of charge and discharge resistance is 1.7~7mΩ. The discharge resistance of the low SOC suddenly increased to 6.9mΩ. The charge and discharge resistance is calculated by the equation below [71];

$$R_{discharge} = \frac{\Delta V_{discharge}}{\Delta V_{charge}} = \left| \frac{V_f - V_{init}}{I_f - I_{init}} \right| \tag{1.1}$$

$$R_{charge} = \frac{\Delta V_{charge}}{\Delta V_{charge}} = \left| \frac{V_f - V_{init}}{I_f - I_{init}} \right| \tag{1.2}$$

where V_f is the terminal voltage at the end of charging or discharging, and V_{init} is the terminal voltage at the beginning of charging or discharging. I_f is the current at the end of charging or discharging, and I_{init} is the current at the beginning of charging or discharging.

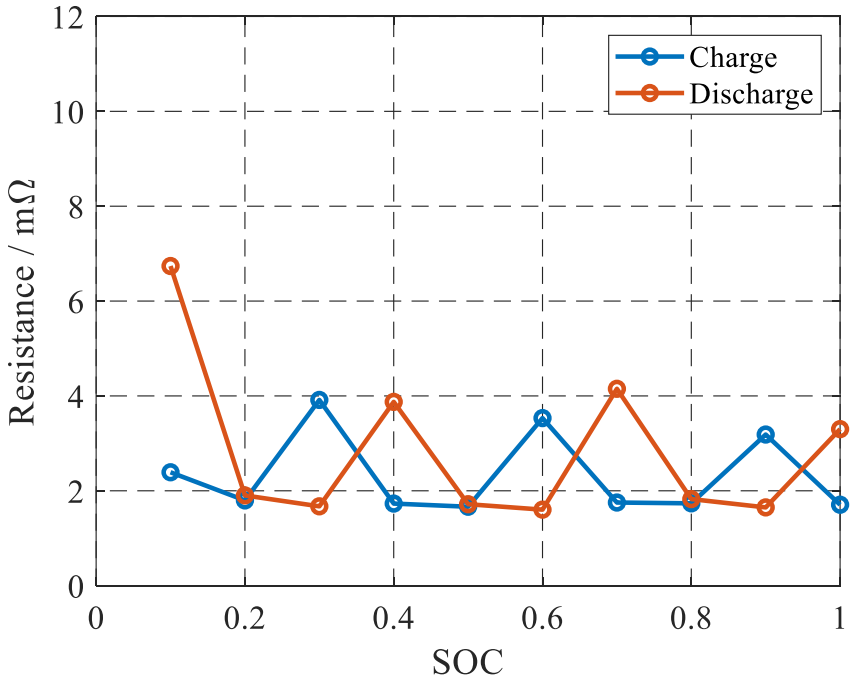

Figure 17. Resistance of charge and discharge as a function of SOC.

(3) Electrochemical Impedance Spectroscopy (EIS)

EIS is a powerful non-destructive technology that measures internal impedances at every battery state of degradation and thus monitors battery degradation during cycling [72]. The measurement of the impedances of a cell is determined by calculation of the relationship between alternating current (AC) signal to the cell and its response. The AC signal over a wide frequency range, typically in the kHz to mHz range, thereby generating a characteristic impedance spectrum. There are potentiostatic and galvanostatic methods dependent upon the input and output sources. The potentiostatic EIS, the applied signal is potential, and the measured signal is current. While galvanostatic EIS applies current and measures potential. Since measured potential and current are a function of time at each frequency, the data is transformed using the Fast Fourier Transform (FFT) that results in a impedances form as a complex number

$$Z(\omega) = \frac{E}{I} = Z_0 \exp\left(j\phi\right) = Z_0\left(\cos\phi + j\sin\phi\right) \tag{1.3}$$

where Z is impedance and E is potential and ϕ is a phase angle. The output response is same as the applied sinusoidal function at the same frequency, but the phase is shifted, which cause imaginary part to exist.

The galvanostatic method manufactured from Gamry instruments is employed for the study. The cell is charged by 50% SOC at C/3 CC-CV and rest in the thermal chamber for 1hour. Then, the amplitude of the AC current of 9A is applied to the cell and impedance is measured from 1000Hz to 10mHz. In order to analyze, measured EIS data is fitted with the equivalent circuit model and the result is shown in Figure 18.

X-axis represents the real part of impedance, while the Y-axis does the imaginary part. The EIS equivalent circuit model consist of inductance (L), ohmic resistance (R0), SEI resistance (R1), SEI capacitance (C), and Warburg admittance (W).

The Nyquist plot is further divided in three areas [72]: (1) for high frequency, the geometry of the cell and porosity of the electrode plates produce an inductive effect. The ohmic resistance is represented by the intercept with the real axis. (2) For medium frequency, an RC-parallel branch is related to the radius of semicircle where relaxation of charge carriers at the Solid Electrolyte Interphase (SEI). (3) For low frequency, the model consists of Warburg impedance. A spike appears at the end of the semicircle and corresponds to ion diffusion in the solid state phase.

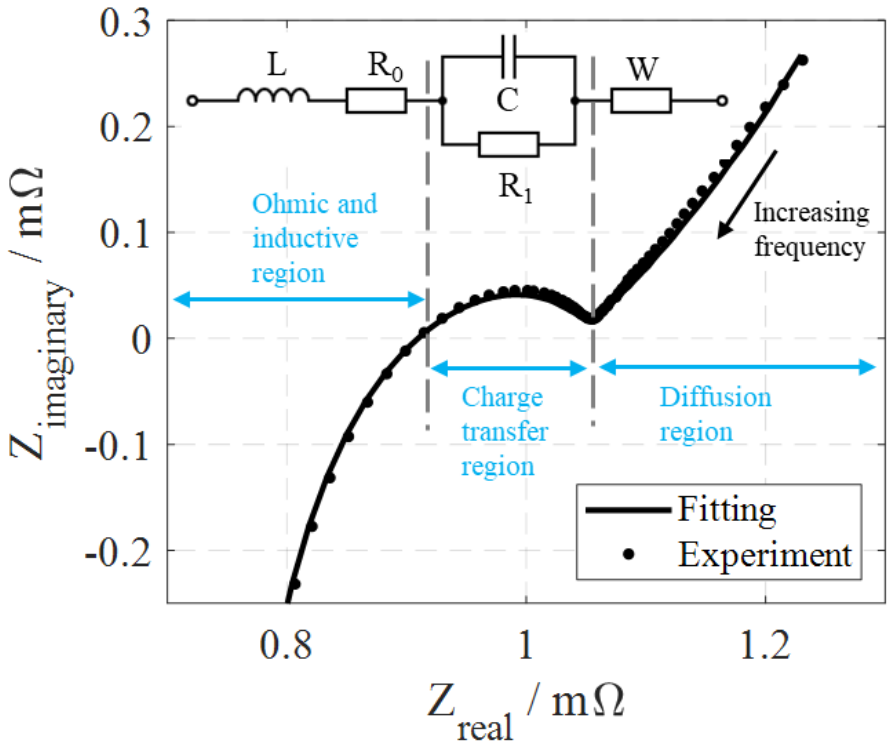

Figure 18. Electrochemical impedance spectroscopy Nyquist plot of a NMCA/graphite-SiO_x cell.

4. Measurement of heat generation rate

4.1 Measurement of entropy coefficient (EC)

The EC is the important parameter for calculation of the reversible heat generation rate. Since the EC is derivative of OCV over temperature, its high accuracy can be achieved by direct measurement. There are potentiometric and calorimetric methods commonly used for determination of the entropy coefficient [73]. The potentiometric method is based on measuring the terminal voltage and temperature in equilibrium state at several SOC points and performed through several stages. First, the cell is fixed at the desired SOC point until reaching an equilibrium state. Then, the terminal voltage is measured by varying temperature of a thermal chamber and measure the dependence between the OCV and the temperature. The method can be described as follows [74];

$$\frac{dU_{OC}}{dT} = \frac{V - V_{init}}{T - T_{init}} \tag{4.1}$$

where V_{init} is the initial terminal voltage, and T_{init} is the initial temperature.

At each SOC point, a certain resting time is required for the cell to reach equilibrium. The relaxation time depends on the thermal properties of a specific cell that is given by the ratio between the heat capacity of the battery and the ability to absorb or emit heat. The papers have attempted to use different durations for relaxation. Although the thermal properties vary depending on the geometry and configuration of the cell, thermal conductivity is directly affected by the cell size , which mainly determines the required duration of relaxation [75],[76],[77],[78].

On the other hand, the calorimetric method allows for simple and fast measurement. The EC is determined by the total heat during charging and discharging based on energy balance [79]. The total heat for charging and discharging is given as below;

$$Q_{total}^{charging} = Q_{irreversible}^{charging} + Q_{reversible}^{charging} \tag{4.2}$$

$$Q_{total}^{discharging} = Q_{irreversible}^{discharging} + Q_{reversible}^{discharging} \tag{4.3}$$

Provided that the irreversible heat is identical during charging and discharging, then the above equation can be rewritten as;

$$Q_{total}^{discharging} - Q_{total}^{charging} = Q_{reversible}^{discharging} - Q_{reversible}^{charging} \tag{4.4}$$

The reversible heat for charging is the negative value of the reversible heat for discharging at the same current density. Therefore, the entropy coefficient is given as below;

$$\frac{dU_{OC}}{dT} = \frac{Q_{total}^{discharging} - Q_{total}^{charging}}{-2IT} \tag{4.5}$$

The potentiometric method is the most accurate and reliable method, but take relative long measurement time and assumes accurate measurement of the heat generation rate Conversely, the calorimetric method does not require a relaxation time, so the measurement time is short, but the application is limited due to expensive equipment, low measurement accuracy and limited space

for increasing size of cells. Therefore, the potentiometric method is typically used for accurate heat prediction [80].

Yang proposed a new method based on Hybridized Time-Frequency Domain analysis (HTFDA), where the EC is determined in time and frequency domain based on the principle of the potentiometric method [81].

HTFDA is divided into two steps, voltage background correction in the time domain and frequency domain analysis. In time domain, the long resting time of the potentiometric method to the equilibrium state is drastically reduced, where the relaxation voltage offset is approximated with a parabolic function in the time domain and then subtract it from the original terminal voltage term. Then, the corrected voltage terms in which the voltage relaxation offset is compensated are obtained. In the frequency domain, a sinusoidal function is applied to the cell and its responses are analyzed using he Fourier transform. The sinusoidal function applied is the temperature, and voltage is also expressed as a function with the same frequency response as temperature. Then, the coefficient of the first harmonic contains the entropy coefficient term and the equation determines the entropy coefficient. The sign of the entropy coefficient is defined in the phase angle between temperature and corresponding voltage.

4.1.1 Selection of optimal parameter

Pre-testing is required to obtain optimal parameters of the exciting function for HTFDA that includes determination of the equivalent temperature change rate (ETCR) and the appropriate temperature amplitude.

The temperature amplitude needs to be selected that determines the entropy coefficient obtained from changes in the frequency domain. If the amplitude is too small, the response in the

frequency domain is too small to analyze. Otherwise, the measurement time takes too long and deteriorates he battery performance. Therefore, compared with the reference, 10°C was selected.

After the operating temperature for the cell was set at 25°C, the cell is rested for 10 hours until an equilibrium state is reached. Then, in order to determine the ETCR, the temperature and voltage response under various conditions were examined considering the heat capacity of the cell and the capability of the calorimeter. Figure 19 (a) shows the temperature response of each ETCR (0.5, 1, 1.5, 2°C/min) of the 1 period sinusoidal temperature profile, whereas the solid line is the input value, and the dashed line is the average temperature of the battery surface. The ETCR of the blue, green, red, and black lines is 2, 1.5, 1, and 0.5°C/min., respectively. As the ETCR increases, the measurement time can be reduced. At 2°C/min, one period of sinusoidal excitation takes less than 20 minutes. At the same time, given the sinusoidal temperature profile, the average temperature of the cell surface should follow the calorimeter's temperature control. However, since the cell used in the experiment is so large that the regulation performance is limited. As shown in Figure 19 (a), when ETCR is greater than 1.5°C/min, the regulation performance of the calorimeter drops, where a delay is observed that does not draw an accurate sinusoidal waveform. Therefore, 1 and 0.5°C/min were selected for the experiments, and the corresponding voltage response is shown in Figure 19 (b). Both profiles were changed with ETCR. As the temperature change is slow, the measurement takes more time in addition to increased noise. Therefore, 1°C/min was selected for ETCR, which takes twice the measurement time.

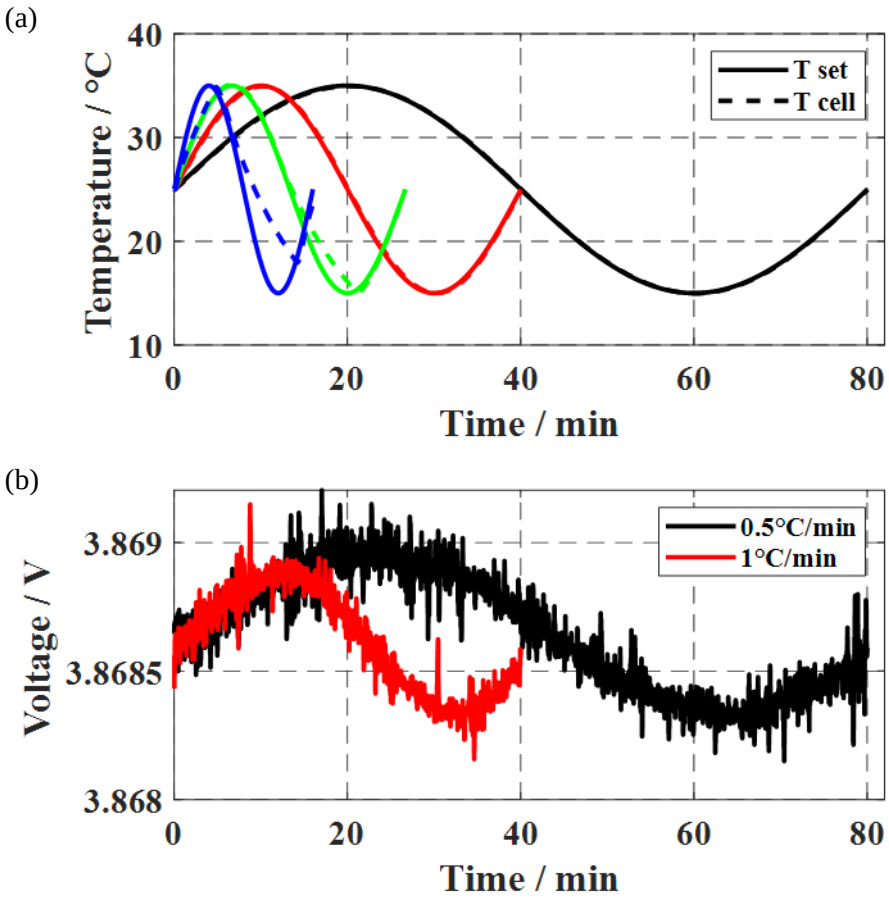

Figure 19. Comparison of (a) average surface temperature response corresponding sinusoidal temperature excitation at different ETCR: 0.5, 1, 1.5, and 2°C/min and (b) voltage response for ETCR: 0.5 and 1°C/min.

4.1.2 Measurement

(1) Figure 20 shows a flow chart that describes the overall procedure of the measurement. Detailed descriptions are as follows; Fully charge the cell using the 0.1C constant current – constant voltage (CC-CV) mode;

(2) Rest for 30 minutes so that the voltage reaches the equilibrium state;

(3) Apply a series of sinusoidal temperature excitations with 2 cycles of ETCR = 1°C/min , ΔT = 10°C;

(4) Rest for 10 minutes to relieve the surface temperature of the cell;

(5) Discharge the cell to target SOC (ΔSOC = 5%) using constant current (CC) mode, and then repeat the same process starting from (2);

The discharge time was calculated by the 0.1C CC discharge at 25°C. The experiment was conducted at a total of 21 SOC points. Using the measured data, the entropy coefficient is determined by 2 steps in time and frequency domain. The measured temperature, which is the average of the thermocouple placed to every three segments and embedded in the Heat flux sensor, and data were collected in a TDMS file via the DAQ system at a sampling rate of 2Hz. Since a battery is hard to fully charge by CC charging, the potentiometric method generally prefers the measurement during discharging. Table 8 includes the parameters selected for the measurement.

Table 8. Parameters of HTFDA

Parameters	**HTFDA**
SOC/ %	5
T_0/ °C	0-45
ΔT/ °C	10
ETCR/ °C/min	1
Measurement duration per/ SOC/h	2.5

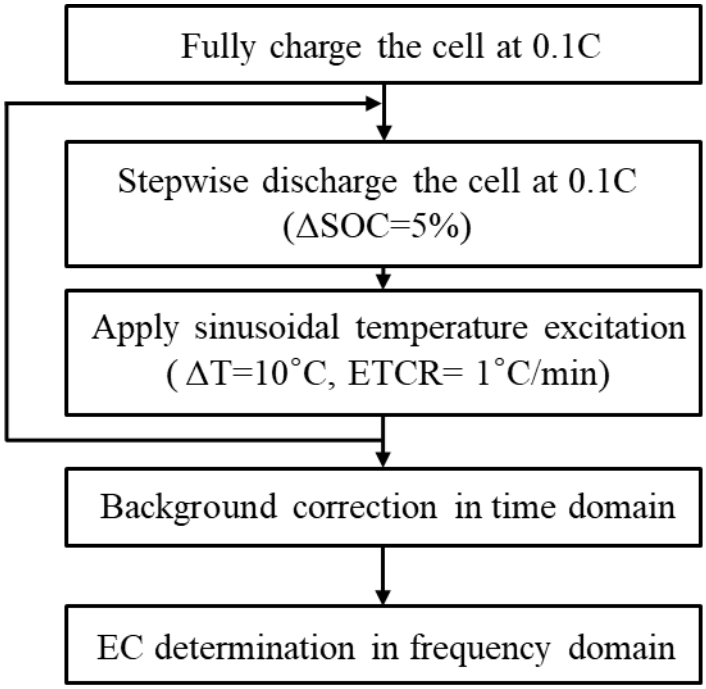

Figure 20. Procedure of HTFDA method for entropy coefficient measurement.

4.1.3 Time and frequency domain analysis

According to the typical potentiometric method, the cell should have reached an equilibrium state before start of a measurement, but HTFDA allows for the measurements before reaching an equilibrium. When a sinusoidal temperature profile is applied to the cell, the terminal voltage reacts in a non-equilibrium state and follows the applied temperature profile, with offset and delay. The voltage offset is used to correct the offset and delay using a polynomial function obtained by a curve fitting. Figure 21 (a) shows the measured waveforms with the corrected voltage at 80% SOC. The solid red line is the measured voltage when the sinusoidal profile of 2 periods is applied to temperature, and the solid blue line is the voltage after voltage background correction. The black dash line shows is the voltage relaxation expressed as a polynomial function. The corrected voltage, in the blue line is obtained by subtracting the offset from the measured voltage,

which eliminates the voltage relaxation term, so like the potentiometric method, a long lasting relaxation time is no more required. Figure 21 (b) shows the frequency spectra for the terminal voltages that include fundamental and harmonics.

As results, the voltage measured by the sinusoidal temperature profile is quickly smoothed by drastically reducing the duration of the relaxation phase to 30 minutes.

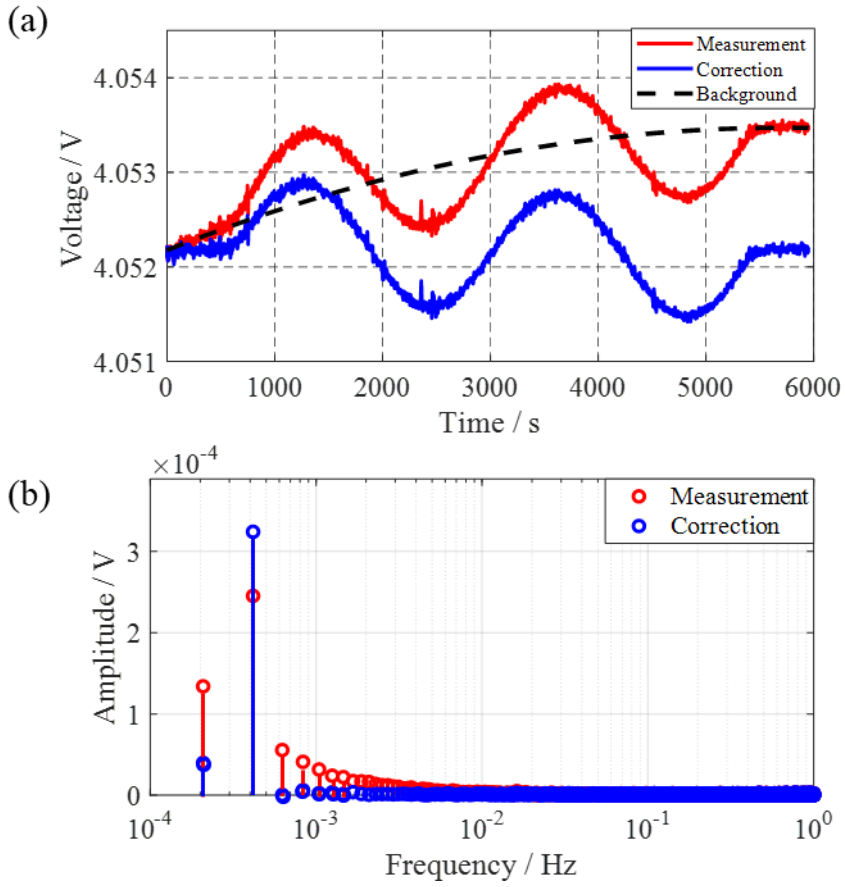

Figure 21. At 80% SOC, (a) measured voltage, background offset and voltage after correction, and (b) the corresponding frequency spectra.

4.2 Result

Figure 22 shows measured temperature and voltage after the background correction, with corresponding frequency spectra at 80% SOC. Figure 22 (a) shows that the sinusoidal temperature excitation profile (solid black line) and the measured average temperature (red dash line) match well within 3% of the error. Figure 22 (b) is the voltage processed after removing the relaxation offset, which changes linearly without delay during the temperature phase change in Figure 22 (c).

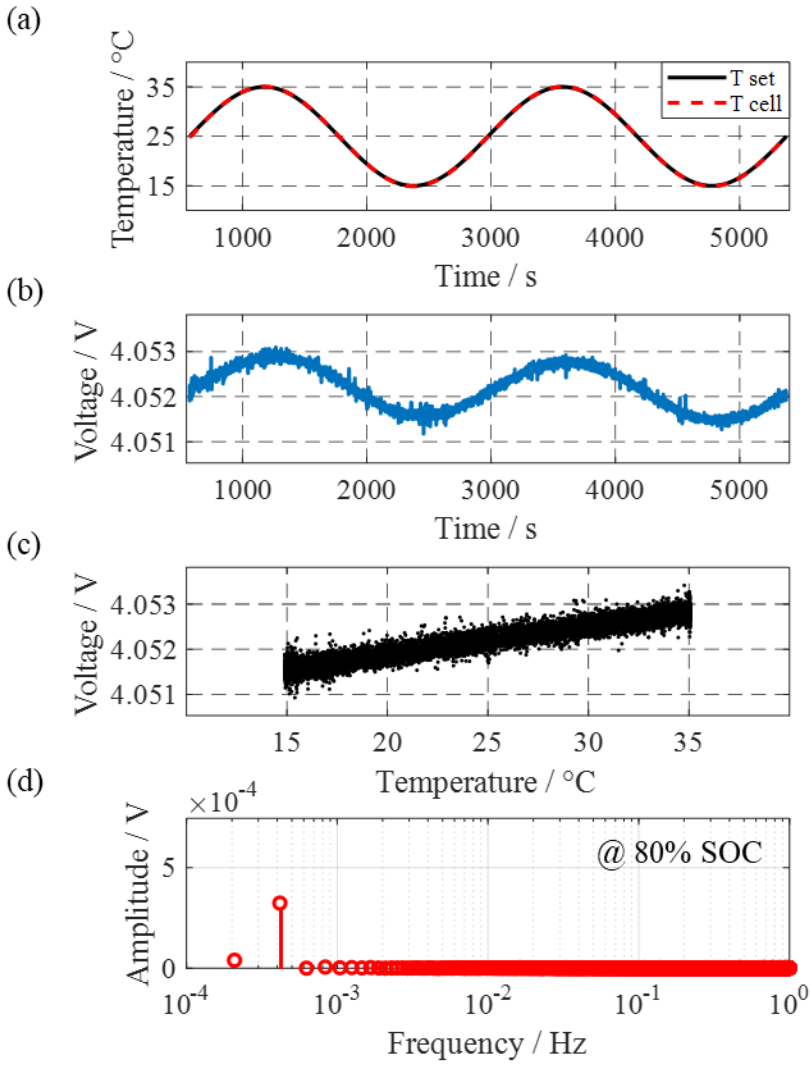

Figure 22. At 80% SOC, (a) average temperature of the cell surface, (b) voltage after background correction, (c) voltage as a function of temperature, (d) frequency spectra corresponding to the sinusoidal profile

Figure 23 shows the measured EC of the NMCA/graphite cell at different SOC using HTFDA. The blue and orange line is the ES during charging and discharging. Both data have similar shapes over most of the SOC range. There is a flat plateau around 0.42 to 0.6 SOC and changes a sign at 0.38 SOC. The sign change indicates a transition between endothermic and exothermic reversible heat generation. Discharge may lead to an endothermic reaction from the reversible losses in a positive region. The phase of discharge is greater between 0.3 and 0.6 SOC. Hysteresis occurs according to OCV profile in the low SOC range. Based on the OCV curve measured during charging, the curve is steeper than discharge curve between 0.2 and 0 SOC, which means the deviation of the charge OCV becomes larger. Therefore, the EC either rapidly decrease or increases. Since most of the studies using the potential method are only measured in the discharge direction, this thesis has focused on analysis of effects of temperature and degradation using the measured entropy coefficient of discharge direction.

The EC is related to the lithium-ion intercalation into the negative and positive electrode materials. The entropy change of a full cell takes place due to the reaction in which the entropy change of negative and positive materials coexist. Yun et al. [82] analyzed the entropy change of NMC/graphite cell by comparing the effects of the cathode and canoed electrodes. The entropy coefficient range from -0.1 to 0.03mV/K for NMC and -0.37 to -0.18mV/K for graphite, and the sign is the opposite. Graphite is a large deviation compared to NMC in terms of structure. In other words, the EC of the full cell is determined by the graphite electrodes. In previous studies, entropy changes in graphite were observed according to structural properties [74],[83]. Empty graphite

lattice can be considered to be very ordered, and li-ion intercalation occurs between the graphene layers in an orderly rather than randomly. This phenomenon is a staging process.

Therefore, the magnitude and trend of the measured EC should be similar to the previous studies, so the result has good agreement [74],[82],[84].

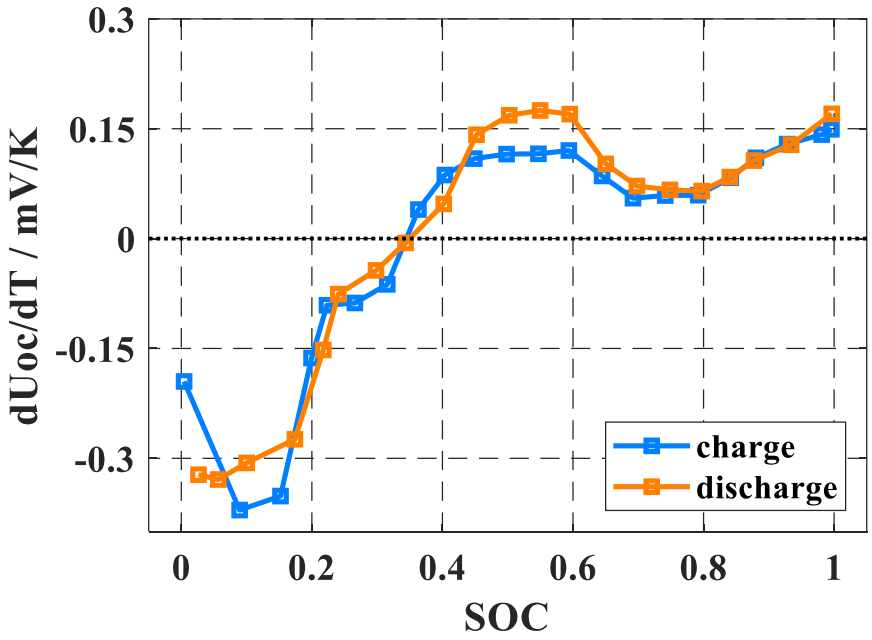

Figure 23. Entropy coefficient of a NMCA/graphite-SiO_x cell 25°C as a function of SOC during charge and discharge.

The operating temperature affects battery performance. The acceptable temperature range for a proper operation of lithium-ion batteries have been suggested. Ji et al. [85] showed that the optimal temperature range for lithium-ion batteries is -20 to 60°C. Based on the recommended temperature range, the measurement temperature was chosen from 0 to 45°C.

Figure 24 shows the EC at various temperatures (0, 15, 25, 35, and 45°C) with different SOCs, where the same NMCA/graphite-SiO_x cell previously used was used again, and the ambient temperature was set by a thermal chamber. For each experiment, the temperature of the cell was

adjusted to the reference temperature and then the experiment was started after a resting time of 1 hour. At a reference temperature, the cell is charged at C/3 CC-CV and discharged at C/3 CC, and discharge capacity is calculated using Coulomb counting. The capacity was measured twice with the same profile, and the average of the two discharge capacity was used to set the C/10 CC discharge time. Then, the entropy coefficient was measured every 5% SOC from fully charged to fully discharged.

Over SOC range, the ECs has the same shapes and do not show any significant changes at different temperatures, which indicates that the reversible heat is not significantly affected by operating temperatures between 0 and 45°C. The range is -0.35 to 0.15 mV/K, and a sign change appears around 0.35 to 0.4 SOC. In the low SOC range, the absolute value tends to increase as the reference temperature increase.

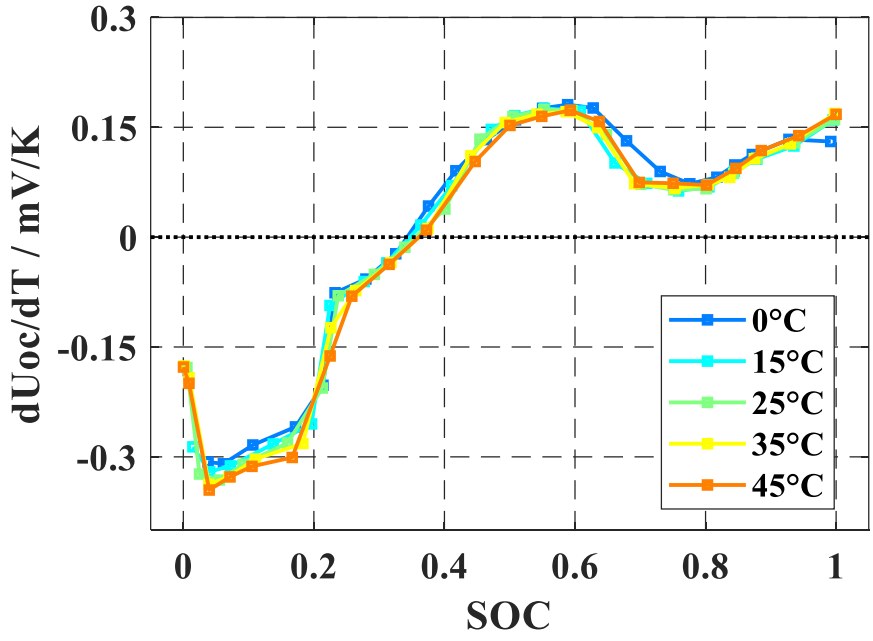

Figure 24. Entropy coefficient at different temperatures (0, 15, 25, 35, and 45°C) as a function of SOC.

The entropy coefficient profiles of an NMCA/graphite cell at different aging conditions are plotted in Figure 25. The cell was cycled with C/2 CC-CV charging and C/2 discharging at 25°C. The capacity of the cell was measured as the discharge capacity by C/3 CC-CV charging and C/3 CC discharging at 25°C. After 300 and 450 cycles of the aging test, the capacity fade (CF) reached 4.7% and 11.1%, respectively. The trends of the EC for the three states are similar. The range from -0.38 to 0.27 mV/K. as the capacity decreased, the absolute value decreased overall in the SOC range. In the 11.1% capacity fade state, the entropy coefficient has a noticeable difference from the 0% and 4.7% profiles; (1) extreme high SOC, (2) extreme low SOC (3) between 0.62 and 0.8 SOC. Yun et al. [82] attempted to r estimate EC for the lithium-ion intercalation state, where the EC t was determined by calculating the intercalated state of the negative electrode before and after cycling. In addition, after the cycle, the lithium-ion intercalated depth loss of the negative electrode is greater than the positive, which means the negative electrode is the dominant degradation factor.

In order to more clearly investigate the effect of aging conditions on the EC, future work will include measurement of the EC when the cell is further aged.

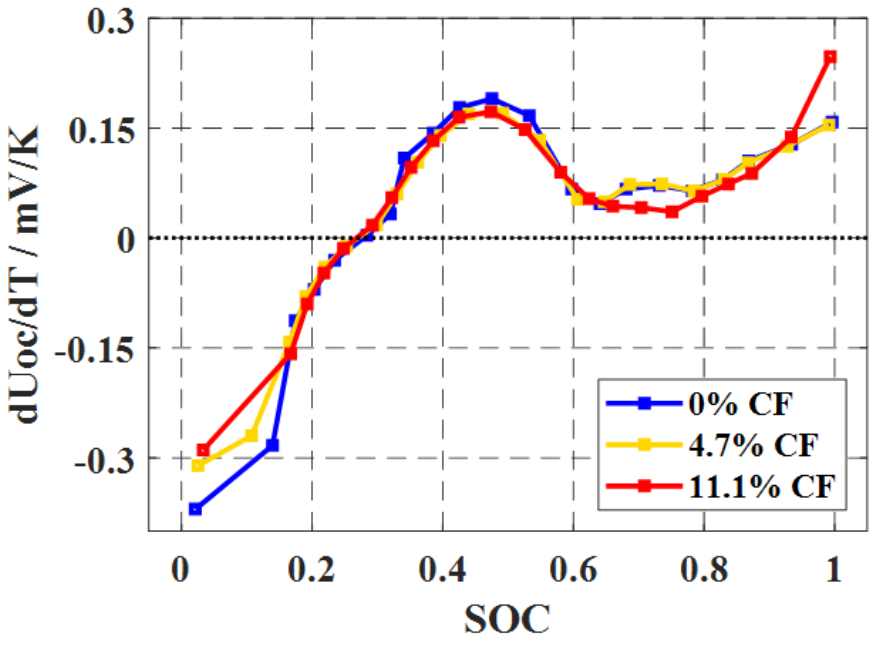

Figure 25. Entropy coefficient of Li(NiMnCoAl)O_2/graphite-SiO_x cell at different aging conditions.

Figure 26 shows the comparison of entropy coefficient profiles with NMCA/graphite cell (blue line) and NMCA/graphite-SiO_x (black line) cell versus different SOC at 25°C. The two cells have the same dimension as 580mm (L)*112.4mm (W)*9.0mm (T). The cathode electrode material of both cells is the same as NMCA, but the anode electrode material is made of graphite and graphite-SiO_x differently. The phase and shape of the EC are similar. However, the deviation occurs due to the entropy coefficient being related to the active material. The entropy coefficient of the NMCA/graphite-SiO_x cell represents to be shifted to the right compared with NMCA/graphite cell.

Therefore, it is worthy of o analyzing the theoretical correlation between the anode materials and the entropy change.

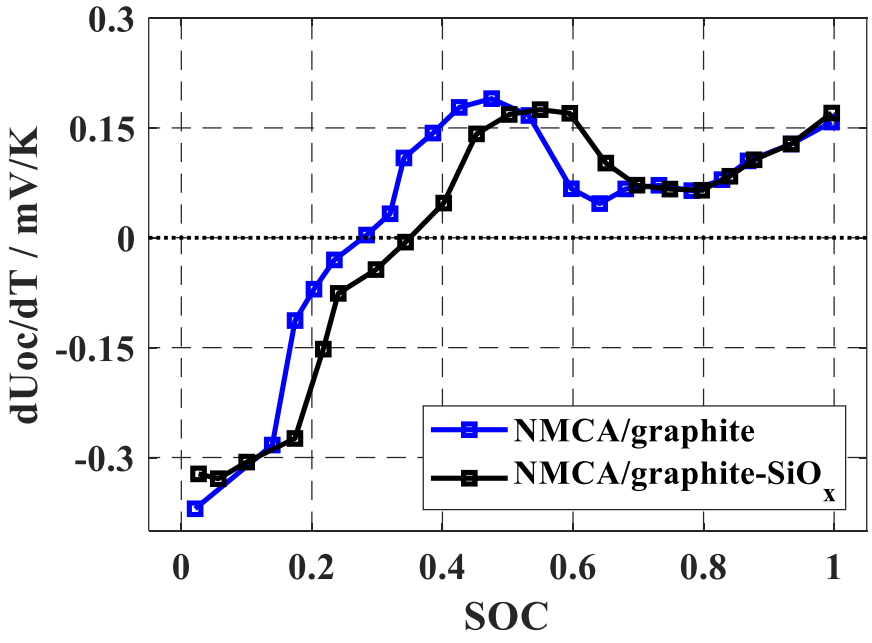

Figure 26. Entropy coefficient of Li(NiMnCoAl)O_2/graphite and Li(NiMnCoAl)O_2/graphite-SiO_x cell.

4.3 Measurement of heat generation rate

Figure 27 shows the measured HGR during charging and discharging at different C rates. After the calorimeter is integrated into a test station, the calorimeter is placed in the thermal chamber to set, and the ambient temperature and the desired initial temperature and the cell is rested for an hour to reach an equilibrium state. Then, the HGRs are measured and compared to each other to quantify the effects of the C rate and temperature on HGR.

- The temperature is set to 25°C, the HGRs are measured and compared when charging and discharging at different C rates. The considered C rates were C/5, C/3, C/2, and 1C.
- The HGRs at different temperatures is measured when charging and discharging at 1C. The considered temperature were 0°C, 15°C, 25°C, 35°C and 45°C, where the cell is charged with CC-CV mode, and discharging was performed by constant current mode.

When charging in CC-CV mode at different C rates, all profiles were run after 2 hours rest period to allow the cell to equilibrate before starting charging or discharging. When the battery reaches 4.2 V, the charging mode changes from CC to CV mode and continues until the current reaches C/20. When discharging in CC mode at different C rates, the cell is fully discharged until reaching the discharge voltage limit of 2.5V.

Figure 27 (a) and (b) show the comparison between the experiment data (dash line) of HGR and the calculated (solid line) using the thermal model explained the previous chapter, which are in good agreement each other. The calculated HGR uses the measured I, T, and entropy coefficients. The difference between the beginning of charging and discharging with the calculated HGR is caused by thermal conductivity that is not considered. In addition, in the real system, the residual

heat of the battery still exists immediately after the completion of charging and discharging, so the measured HGR decreases gradually like an exponential function due to the thermal time constant inherent in the calorimeter.

HGR during charging and discharging increases as the current increases. The peak of HGR for discharging is greater than charging at the same C rate. For example, the peak of HGR for charging and discharging at 1C CC mode is 38W and 70W. In addition, HGR for discharging is greater than that at charging, which is caused by the exothermal or endothermal process of reversible heat. However, the irreversible heat source is exothermic regardless of charging or discharging. As the current increases, irreversible heat is the dominant part.

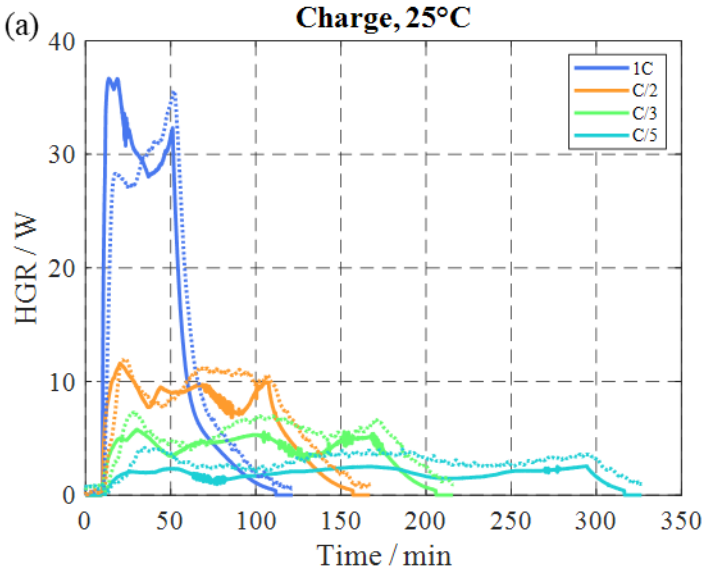

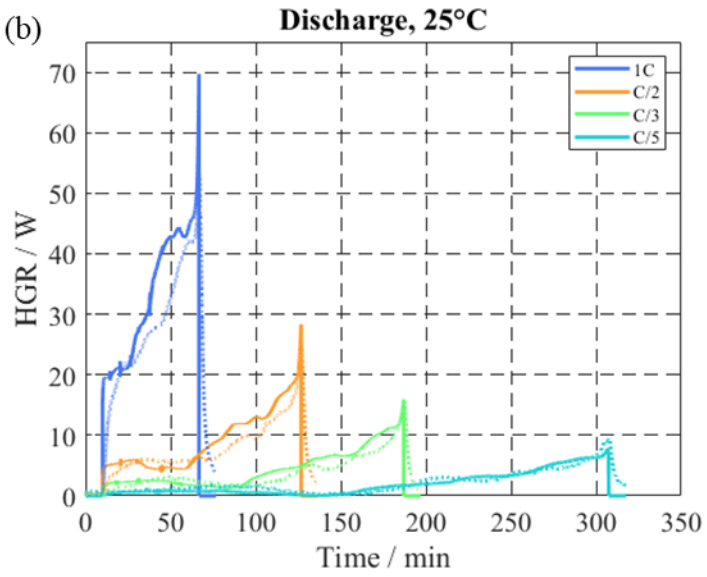

Figure 27. Measurement result of HGR at different C rates: 1C, C/2, C/3 and C/5 under (a) CC-CV charging and (b) CC discharging at 25°C.

Figure 28 (a) and (b) show HGR during for charging and discharging at 0°C, 15°C, 25°C, 35°C, and 45°C. When the initial temperature of the battery is set, the experiment is conducted after 30 minutes of rest until the cells reach equilibrium. The cell is charged by CC-CV and discharged by CC. Comparing the amount of HGR during charging and discharging at the overall temperature, more HGR was generated while discharging. As the temperature decreases, the HGR increase rapidly due to the increased Ohmic and SEI resistances. As a result, irreversible heat becomes the most dominant heat source.

On the other hand, as high temperatures rise, reversible heat sources affected by entropy changes become dominant because of the low internal resistance of the battery [86]. In addition, the effect of temperature is more obvious in the temperature of 35 and 45°C profile shapes. At 0°C, the HGR tends to increase during CC mode. Conversely, according to the profile of 35 and 45°C, the heat increases rapidly due to a large current that suddenly flows at the start of the charge.

However, the HGR decreases sharply between 20-30Ah and 50-60Ah because of the affected reversible HGR. The sign change of the EC occurs at these two points that indicates a transition from the exothermic to the endothermic process. This same phenomenon takes place in the discharge EC profile at high temperatures, even around 30, 60, 80, and 95Ah. Thus, the EC is the critical parameter that should be considered in predicting the amount of HGR.

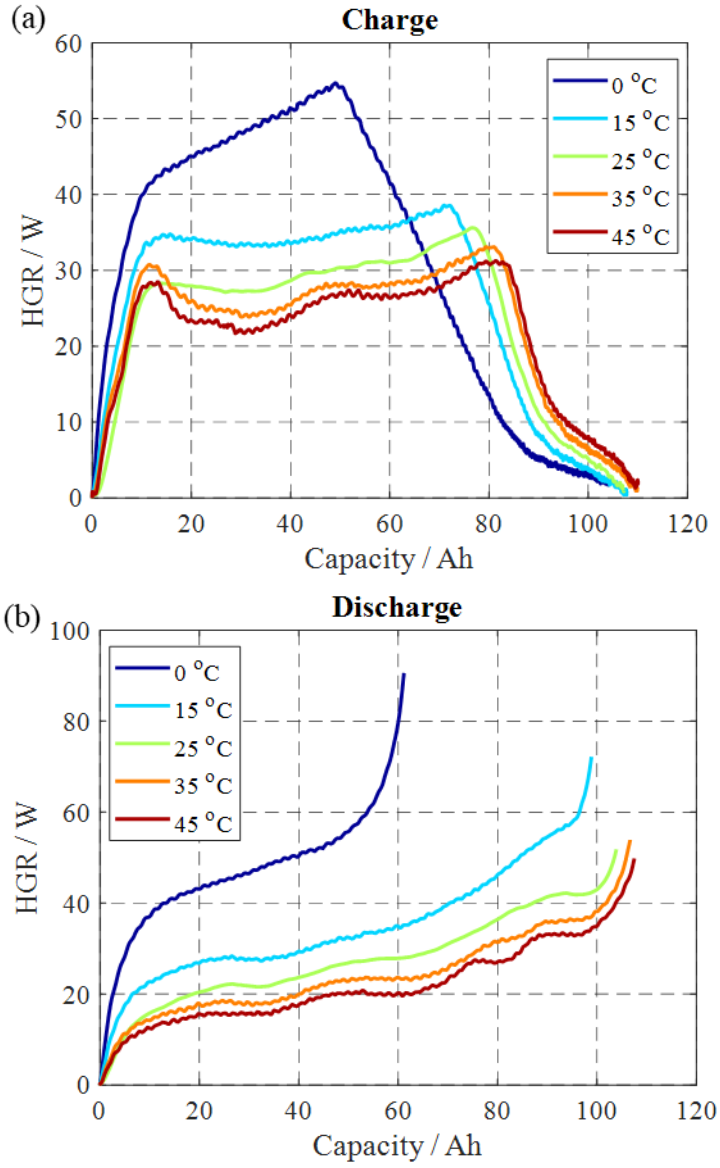

Figure 28.Measurement result of HGR at different temperatures: 0, 15, 25, 35, and 45°C under (a) CC-CV charging and (b) CC discharge at 1C

According to energy conservation, the chemical potential energy generated by the transport of ions inside the battery is the sum of electrical energy and heat. Hence, efficiency can be calculated from the ratio of electrical energy as input to total energy as output [87],[6].

$$Energy \quad efficiency_{ch} = \frac{\int_0^t HGR_{ch}\, dt}{\int_0^t V \cdot I\, dt} \times 100 \tag{4.6}$$

$$Energy \quad efficiency_{dch} = \frac{\int_0^t HGR_{dch}\, dt}{\int_0^t HGR_{dch}\, dt + \int_0^t V \cdot I\, dt} \times 100 \tag{4.7}$$

where V is terminal voltage and I is current.

Figure 29 shows the comparison of electric energy, total heat, and energy efficiency during charging and discharging at 25°C with different C rates.

As the C rate for charge and discharge increases, the electric energy decreases due to overpotentials. However, the irreversible heat increases and the total amount of heat generated increases. The total amount of heat generated during charging is greater than that during discharging at C/5, C/3, and C/2, as shown in Figure 29. The peak of the measured HGR during discharging is greater than charging, but the average HGR during operation is greater when charging. The further experimental investigation is needed to analyze the total heat generation of charge and discharge rates with a rate profile that is larger than 1C. As shown in Figure 29 (a.3) and (b.3), the ratio of electrical energy loss increases as the C rate increases.

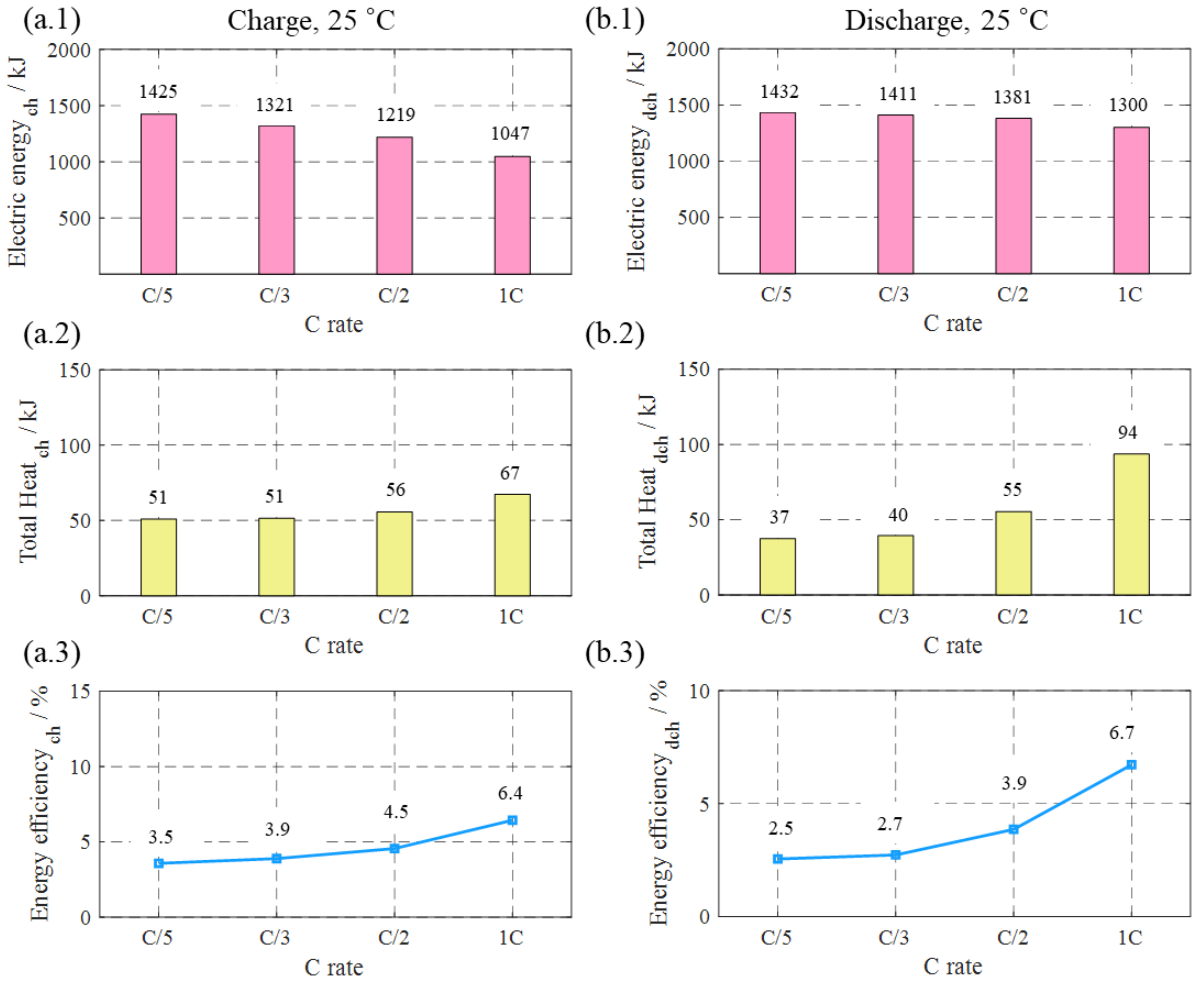

Figure 29. Comparison of electric energy, total heat, and energy efficiency for charging (a.1)-(a.3) and for discharging (b.1)-(b.3) at different C rates.

The electric energy, total heat, and energy efficiency of 1C charge and discharge at different operating temperatures are shown in Figure 30. As the temperature increases, the electrical energy for both charging and discharging increases. In addition, the total heat generation increases from 0 to 15°C and decreases from 25°C to 45°C due to the decreased internal resistance at high temperatures. At low temperatures, the Ohmic overpotential increases and the time for the voltage to reach the cut-off voltage becomes shorter. Thus, the total heat decreases at lower temperatures due to the decrease discharging time. Therefore, energy efficiency decreases with

increasing temperature. At 0°C, the efficiency at charge and discharge is 58% and 48% greater than those at 45°C, respectively.

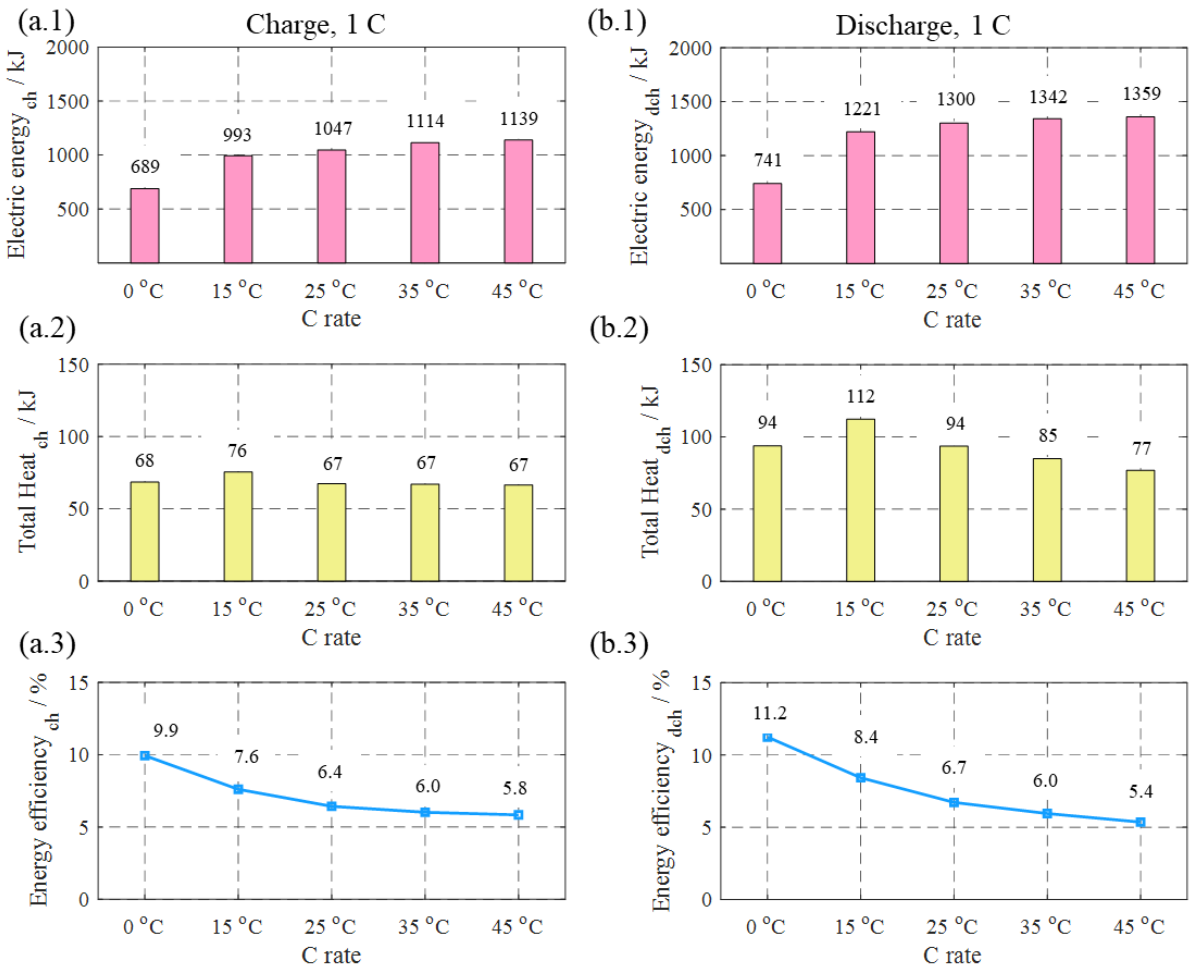

Figure 30. Comparison of electric energy, total heat, and energy efficiency for charging (a.1)-(a.3) and for discharging (b.1)-(b.3) at different temperatures.

5. Conclusion

5.1 Conclusion

In this thesis, the basic principle for heat generation is studied by reviewing published papers and experimental investigations. The HGRs of a large format pouch type lithium ion battery at various operating conditions were measured using the developed calorimeter and analyzed. The experiment results are compared with a thermal model, which are in a good agreement with each other.

- In the introduction to the work, the electrochemical characteristics, packaging design, and charging/discharging methods of various secondary rechargeable batteries were reviewed. Since battery performance is dominantly affected by operation and storage temperature, three ranges are considered, low, high, and non-uniform temperature distribution.
- A test station was developed that facilitates the experimental characterization of the thermal behaviors of a battery cell. A high accuracy data can be collected at any single or combined charging and discharging profile. In addition, potential overcharge and overdischarge of the cell are monitored and prevented by an extra PLC unit. A developed calorimeter measures the HGR of a cell during charging or discharging that consists of two TEAs in a sandwich structure. Three heat flux sensors are placed at the cell side of the metal plate and generate the output voltage proportional to the heat flow between the cell surface and the metal plate during charging or discharging. The collected output data is processed to calculate the HGR under consideration of the calibration coefficient obtained by the calibration process.

- The heat generated in an operating cell can be divided into two sources, irreversible and reversible heat. The reversible part is dominantly affected by EC. Therefore, the EC was measured by HTFDA and used to predict the total heat accurately. In addition, HTFDA was compared with the calorimetric and potentiometric methods, which are the widely used measurement methods. HTFDA reduces the measurement time by more than 60% with acceptable accuracy compared to the potentiometric method. Hysteresis behavior is generally present in cells with Si anode chemistry. The investigation shows that the behavior is present in the low SOC region as in the OCV. The effects of anode active material, temperature, and aging on EC are studied.

- The heat measured by the calorimeter was at various C rates and temperatures.

    - ✓ The various C rates include C/5, C/3, C/2, and 1C at 25°C during charging and discharging. The larger the C rate, the larger the Joule heating that contributes to the main heat source. Conversely, the smaller the C rate is, the more rapidly increases the influence of the reversible heat and becomes the dominant part. At the same C rate, the HGR during charging is always less than that during discharging because of the contribution of the reversible heat during discharging.

    - ✓ Various temperatures include 0, 15, 25, 35, and 45°C during 1C CC charging and discharging. At low temperatures, the HGR increases rapidly due to the increased ion centration difference within particles and contact resistance [88]. The reversible thermal part is the main heat source at elevated temperatures because of eased chemical reactions and the associated high ion conductivities. HGR decreases as the temperature increases. The effect of the C rate and temperature of electrical energy, total heat, and energy efficiency is shown in a bar graphically.

5.2 Future work

- In this study, we investigated the effect of C rate and temperature on HGR. Furthermore, the effect of non-uniform temperature distribution will be analyzed experimentally. For this study, the calorimeter applies different temperatures to the three segments of the cell: positive electrode side, negative electrode side, and center. In addition, the effect on battery degradation could be observed by comparing the battery capacity fade after performing the same cycle profile under uniform and non-uniform temperature distribution conditions.

- A relatively simple thermal model is used to predict the HGR. Future work includes investigating the development of an electrochemical model to estimate the thermal behavior of lithium-ion batteries accurately. Additionally, it is necessary to understand the electrochemical characteristics of the inside of the battery.

Reference

[1] IEA, “Global Energy Review 2020,” 2020. doi: 10.1787/a60abbf2-en.

[2] V. Masson-Delmotte *et al.*, “Global warming of 1.5°C An IPCC Special Report on the impacts of global warming of 1.5°C above pre-industrial levels and related global greenhouse gas emission pathways, in the context of strengthening the global response to the threat of climate change, sustainable development, and efforts to eradicate poverty Edited by Science Officer Science Assistant Graphics Officer Working Group I Technical Support Unit,” 2022, doi: 10.1017/9781009157940.

[3] I. Energy Agency, “World Energy Outlook Special Report Africa Energy Outlook 2022,” 2022.

[4] B. Bose, A. Garg, B. K. Panigrahi, and J. Kim, “Study on Li-ion battery fast charging strategies: Review, challenges and proposed charging framework,” *Journal of Energy Storage*, vol. 55, Nov. 2022, doi: 10.1016/J.EST.2022.105507.

[5] M. S. Patil, J. H. Seo, S. Panchal, S. W. Jee, and M. Y. Lee, “Investigation on thermal performance of water-cooled Li-ion pouch cell and pack at high discharge rate with U-turn type microchannel cold plate,” *International Journal of Heat and Mass Transfer*, vol. 155, Jul. 2020, doi: 10.1016/J.IJHEATMASSTRANSFER.2020.119728.

[6] Y. Hu, S. Y. Choe, and T. R. Garrick, “Measurement of heat generation rate and heat sources of pouch type Li-ion cells,” *Applied Thermal Engineering*, vol. 189, May 2021, doi: 10.1016/j.applthermaleng.2021.116709.

[7] A. M. Ahmad, G. Thenaisie, and S. G. Lee, “A calorimetric approach to fast entropy-variations extraction for lithium-ion batteries using optimized galvanostatic intermittent titration technique,” *Journal of Power Sources Advances*, vol. 16, p. 100097, Aug. 2022, doi: 10.1016/J.POWERA.2022.100097.

[8] K. Chen, G. Unsworth, and X. Li, “Measurements of heat generation in prismatic Li-ion batteries,” *Journal of Power Sources*, vol. 261, pp. 28–37, Sep. 2014, doi: 10.1016/J.JPOWSOUR.2014.03.037.

[9] Y. Yin, Z. Zheng, and S. Choe, “Design of a Calorimeter for Measurement of Heat Generation Rate of Lithium Ion Battery Using Thermoelectric Device,” *SAE Int. J. Alt. Power*, vol. 6, no. 2, p. 2017, doi: 10.4271/2017-01-1213.

[10] A. Tomaszewska *et al.*, “Lithium-ion battery fast charging: A review,” *eTransportation*, vol. 1, p. 100011, Aug. 2019, doi: 10.1016/j.etran.2019.100011.

[11] Y. Ji, Y. Zhang, and C.-Y. Wang, “Li-Ion Cell Operation at Low Temperatures,” *J. Electrochem. Soc.*, vol. 160, no. 4, p. A636, Feb. 2013, doi: 10.1149/2.047304jes.

[12] M. Rosa and P. Palacı´n, “Recent advances in rechargeable battery materials: a chemist’s perspective,” *Chemical Society Reviews*, vol. 38, no. 9, pp. 2565–2575, Aug. 2009, doi: 10.1039/B820555H.

[13] Y. Liang *et al.*, “A review of rechargeable batteries for portable electronic devices,” *InfoMat*, vol. 1, no. 1, pp. 6–32, Mar. 2019, doi: 10.1002/INF2.12000.

[14] C. D. Rahn and C. Y. Wang, “Battery Systems Engineering,” *Battery Systems Engineering*, Jan. 2013, doi: 10.1002/9781118517048.

[15] J. Xiao *et al.*, “Understanding and applying coulombic efficiency in lithium metal batteries,” *Nature Energy*, vol. 5, no. 8, pp. 561–568, Aug. 2020, doi: 10.1038/s41560-020-0648-z.

[16] Q. Wang, B. Jiang, B. Li, and Y. Yan, “A critical review of thermal management models and solutions of lithium-ion batteries for the development of pure electric vehicles,”

Renewable and Sustainable Energy Reviews, vol. 64. Elsevier Ltd, pp. 106–128, Oct. 01, 2016. doi: 10.1016/j.rser.2016.05.033.
[17] I. Buchmann, “Batteries in a portable world : a handbook on rechargeable batteries for non-engineers,” p. 360.
[18] J. Zheng, W. H. Kan, and A. Manthiram, “Role of Mn Content on the Electrochemical Properties of Nickel-Rich Layered LiNi0.8–xCo0.1Mn0.1+xO2 ($0.0 \leq x \leq 0.08$) Cathodes for Lithium-Ion Batteries,” *ACS Appl. Mater. Interfaces*, vol. 7, no. 12, pp. 6926–6934, Apr. 2015, doi: 10.1021/acsami.5b00788.
[19] G. W. Nam *et al.*, “Capacity Fading of Ni-Rich NCA Cathodes: Effect of Microcracking Extent,” *ACS Energy Lett.*, vol. 4, no. 12, pp. 2995–3001, Dec. 2019, doi: 10.1021/acsenergylett.9b02302.
[20] A. F. Léonard and N. Job, “Safe and green Li-ion batteries based on LiFePO4 and Li4Ti5O12 sprayed as aqueous slurries with xanthan gum as common binder,” *Materials Today Energy*, vol. 12, pp. 168–178, Jun. 2019, doi: 10.1016/j.mtener.2019.01.008.
[21] Q. Wang, B. Jiang, B. Li, and Y. Yan, “A critical review of thermal management models and solutions of lithium-ion batteries for the development of pure electric vehicles,” *Renewable and Sustainable Energy Reviews*, vol. 64, pp. 106–128, Oct. 2016, doi: 10.1016/j.rser.2016.05.033.
[22] S. Xia *et al.*, “Chemomechanical interplay of layered cathode materials undergoing fast charging in lithium batteries,” *Nano Energy*, vol. 53, pp. 753–762, Nov. 2018, doi: 10.1016/j.nanoen.2018.09.051.
[23] G. Ning, B. Haran, and B. N. Popov, “Capacity fade study of lithium-ion batteries cycled at high discharge rates,” *Journal of Power Sources*, vol. 117, no. 1, pp. 160–169, May 2003, doi: 10.1016/S0378-7753(03)00029-6.
[24] Z. Xu, M. M. Rahman, L. Mu, Y. Liu, and F. Lin, “Chemomechanical behaviors of layered cathode materials in alkali metal ion batteries,” *J. Mater. Chem. A*, vol. 6, no. 44, pp. 21859–21884, Nov. 2018, doi: 10.1039/C8TA06875E.
[25] W. H. Woodford, W. C. Carter, and Y.-M. Chiang, “Design criteria for electrochemical shock resistant battery electrodes,” *Energy Environ. Sci.*, vol. 5, no. 7, pp. 8014–8024, Jun. 2012, doi: 10.1039/C2EE21874G.
[26] J. P. Pender *et al.*, “Electrode Degradation in Lithium-Ion Batteries,” *ACS Nano*, vol. 14, no. 2, pp. 1243–1295, Feb. 2020, doi: 10.1021/acsnano.9b04365.
[27] M. Weiss *et al.*, “Fast Charging of Lithium-Ion Batteries: A Review of Materials Aspects,” *Advanced Energy Materials*, vol. 11, no. 33, p. 2101126, 2021, doi: 10.1002/aenm.202101126.
[28] S. Ahmed *et al.*, “Enabling fast charging – A battery technology gap assessment,” *Journal of Power Sources*, vol. 367, pp. 250–262, Nov. 2017, doi: 10.1016/j.jpowsour.2017.06.055.
[29] M. Vujković, I. Stojković, M. Mitrić, S. Mentus, and N. Cvjetićanin, “Hydrothermal synthesis of Li4Ti5O12/C nanostructured composites: Morphology and electrochemical performance,” *Materials Research Bulletin*, vol. 48, no. 2, pp. 218–223, Feb. 2013, doi: 10.1016/j.materresbull.2012.09.071.
[30] L. A.-W. Ellingsen, G. Majeau-Bettez, B. Singh, A. K. Srivastava, L. O. Valøen, and A. H. Strømman, “Life Cycle Assessment of a Lithium-Ion Battery Vehicle Pack,” *Journal of Industrial Ecology*, vol. 18, no. 1, pp. 113–124, 2014, doi: 10.1111/jiec.12072.
[31] X.-Y. Yao and M. G. Pecht, “Tab Design and Failures in Cylindrical Li-ion Batteries,”

IEEE Access, vol. 7, pp. 24082–24095, 2019, doi: 10.1109/ACCESS.2019.2899793.
[32] L. E. Asp *et al.*, "A Structural Battery and its Multifunctional Performance," *Advanced Energy and Sustainability Research*, vol. 2, no. 3, p. 2000093, Mar. 2021, doi: 10.1002/AESR.202000093.
[33] T. B. Reddy, *Linden's Handbook of Batteries, Fourth Edition*. McGraw-Hill Education, 2011. Accessed: Nov. 21, 2022. [Online]. Available: https://www.accessengineeringlibrary.com/content/book/9780071624213
[34] R. H. Petrucci, F. G. Herring, J. D. Madura, and C. Bissonnette, *General Chemistry: Principe and Modern Aplication*, vol. 73, no. 11. 2005.
[35] L. K. Willenberg, P. Dechent, G. Fuchs, D. U. Sauer, and E. Figgemeier, "High-Precision Monitoring of Volume Change of Commercial Lithium-Ion Batteries by Using Strain Gauges", doi: 10.3390/su12020557.
[36] R. D. Deshpande and D. M. Bernardi, "Modeling Solid-Electrolyte Interphase (SEI) Fracture: Coupled Mechanical/Chemical Degradation of the Lithium Ion Battery," *Journal of The Electrochemical Society*, vol. 164, no. 2, pp. 461–474, 2017, doi: 10.1149/2.0841702jes.
[37] B. Bose, A. Garg, B. K. Panigrahi, and J. Kim, "Study on Li-ion battery fast charging strategies: Review, challenges and proposed charging framework," *Journal of Energy Storage*, vol. 55, p. 105507, Nov. 2022, doi: 10.1016/j.est.2022.105507.
[38] E. Ayoub and N. Karami, "Review on the charging techniques of a Li-Ion battery," *2015 3rd International Conference on Technological Advances in Electrical, Electronics and Computer Engineering, TAEECE 2015*, pp. 50–55, 2015, doi: 10.1109/TAEECE.2015.7113599.
[39] N. Ghaeminezhad and M. Monfared, "Charging control strategies for lithium-ion battery packs: Review and recent developments," *IET Power Electronics*, vol. 15, no. 5, pp. 349–367, 2022, doi: 10.1049/pel2.12219.
[40] A. B. Khan and W. Choi, "Optimal Charge Pattern for the High-Performance Multistage Constant Current Charge Method for the Li-Ion Batteries," *IEEE Transactions on Energy Conversion*, vol. 33, no. 3, pp. 1132–1140, Sep. 2018, doi: 10.1109/TEC.2018.2801381.
[41] Y. Li, K. Li, Y. Xie, J. Liu, C. Fu, and B. Liu, "Optimized charging of lithium-ion battery for electric vehicles: Adaptive multistage constant current–constant voltage charging strategy," *Renewable Energy*, vol. 146, pp. 2688–2699, Feb. 2020, doi: 10.1016/j.renene.2019.08.077.
[42] B. Škugor and J. Deur, "Dynamic programming-based optimisation of charging an electric vehicle fleet system represented by an aggregate battery model," *Energy*, vol. 92, pp. 456–465, Dec. 2015, doi: 10.1016/j.energy.2015.03.057.
[43] E. Banguero, A. Correcher, Á. Pérez-Navarro, F. Morant, and A. Aristizabal, "A Review on Battery Charging and Discharging Control Strategies: Application to Renewable Energy Systems," *Energies*, vol. 11, no. 4, Art. no. 4, Apr. 2018, doi: 10.3390/en11041021.
[44] T. M. Bandhauer, S. Garimella, and T. F. Fuller, "A Critical Review of Thermal Issues in Lithium-Ion Batteries," *Journal of The Electrochemical Society*, vol. 158, no. 3, p. R1, 2011, doi: 10.1149/1.3515880.
[45] W. Wu, S. Wang, W. Wu, K. Chen, S. Hong, and Y. Lai, "A critical review of battery thermal performance and liquid based battery thermal management," *Energy Conversion and Management*, vol. 182. Elsevier Ltd, pp. 262–281, Jan. 01, 2019. doi:

10.1016/j.enconman.2018.12.051.
[46] P. Ramadass, B. Haran, R. White, and B. N. Popov, “Capacity fade of Sony 18650 cells cycled at elevated temperatures: Part I. Cycling performance,” *Journal of Power Sources*, vol. 112, no. 2, pp. 606–613, Nov. 2002, doi: 10.1016/S0378-7753(02)00474-3.
[47] L. Lu, X. Han, J. Li, J. Hua, and M. Ouyang, “A review on the key issues for lithium-ion battery management in electric vehicles,” *Journal of Power Sources*, vol. 226, pp. 272–288, Mar. 2013, doi: 10.1016/J.JPOWSOUR.2012.10.060.
[48] “Lithium Battery Failures.” https://www.mpoweruk.com/lithium_failures.htm (accessed Nov. 19, 2022).
[49] X. Tian *et al.*, “Design Strategies of Safe Electrolytes for Preventing Thermal Runaway in Lithium Ion Batteries,” *Chem. Mater.*, vol. 32, no. 23, pp. 9821–9848, Dec. 2020, doi: 10.1021/acs.chemmater.0c02428.
[50] D. Burow *et al.*, “Inhomogeneous degradation of graphite anodes in automotive lithium ion batteries under low-temperature pulse cycling conditions,” *Journal of Power Sources*, vol. 307, pp. 806–814, Mar. 2016, doi: 10.1016/J.JPOWSOUR.2016.01.033.
[51] G. Nagasubramanian, “Electrical characteristics of 18650 Li-ion cells at low temperatures”.
[52] M. C. Smart *et al.*, “Improved low-temperature performance of lithium-ion cells with quaternary carbonate-based electrolytes,” *Journal of Power Sources*, vol. 119–121, pp. 349–358, Jun. 2003, doi: 10.1016/S0378-7753(03)00154-X.
[53] M. Ouyang *et al.*, “Low temperature aging mechanism identification and lithium deposition in a large format lithium iron phosphate battery for different charge profiles,” *Journal of Power Sources*, vol. 286, pp. 309–320, Jul. 2015, doi: 10.1016/J.JPOWSOUR.2015.03.178.
[54] W. Wu, W. Wu, and S. Wang, “Thermal management optimization of a prismatic battery with shape-stabilized phase change material,” *International Journal of Heat and Mass Transfer*, vol. 121, pp. 967–977, Jun. 2018, doi: 10.1016/J.IJHEATMASSTRANSFER.2018.01.062.
[55] Y. Yang, X. Hu, D. Qing, and F. Chen, “Arrhenius Equation-Based Cell-Health Assessment: Application to Thermal Energy Management Design of a HEV NiMH Battery Pack,” vol. 6, pp. 2709–2725, 2013, doi: 10.3390/en6052709.
[56] C. Kuper, M. Hoh, G. H. Miller, and J. Fuhr, “Thermal Management of Hybrid Vehicle Battery Systems,” *undefined*, 2009.
[57] C. V. Hémery, F. Pra, J. F. Robin, and P. Marty, “Experimental performances of a battery thermal management system using a phase change material,” *Journal of Power Sources*, vol. 270, pp. 349–358, Dec. 2014, doi: 10.1016/J.JPOWSOUR.2014.07.147.
[58] D. Bernardi, E. Pawlikowski, and J. Newman, “GENERAL ENERGY BALANCE FOR BATTERY SYSTEMS.,” *Electrochemical Society Extended Abstracts*, vol. 84–2, no. 1, pp. 164–165, Jan. 1984, doi: 10.1149/1.2113792/XML.
[59] C. Forgez, D. Vinh Do, G. Friedrich, M. Morcrette, and C. Delacourt, “Thermal modeling of a cylindrical LiFePO4/graphite lithium-ion battery,” *Journal of Power Sources*, vol. 195, no. 9, pp. 2961–2968, May 2010, doi: 10.1016/J.JPOWSOUR.2009.10.105.
[60] Y. Hu, S.-Y. Choe, and T. R. Garrick, “Measurement of two-dimensional heat generation rate of pouch type lithium-ion battery using a multifunctional calorimeter,” *Journal of Power Sources*, vol. 532, p. 231350, Jun. 2022, doi: 10.1016/j.jpowsour.2022.231350.

[61] W. Ai, N. Kirkaldy, Y. Jiang, G. Offer, H. Wang, and B. Wu, “A composite electrode model for lithium-ion batteries with silicon/graphite negative electrodes,” *Journal of Power Sources*, vol. 527, Apr. 2022, doi: 10.1016/j.jpowsour.2022.231142.
[62] G. Dong, J. Wei, C. Zhang, and Z. Chen, “Online state of charge estimation and open circuit voltage hysteresis modeling of LiFePO4 battery using invariant imbedding method,” *Applied Energy*, vol. 162, pp. 163–171, Jan. 2016, doi: 10.1016/J.APENERGY.2015.10.092.
[63] R. Li *et al.*, “Voltage hysteresis of magnesium anode: Taking magnesium-sulfur battery as an example,” *Electrochimica Acta*, vol. 369, p. 137685, Feb. 2021, doi: 10.1016/J.ELECTACTA.2020.137685.
[64] L. Zhu, Z. Sun, H. Dai, and X. Wei, “A novel modeling methodology of open circuit voltage hysteresis for LiFePO4 batteries based on an adaptive discrete Preisach model,” *Applied Energy*, vol. 155, pp. 91–109, Oct. 2015, doi: 10.1016/J.APENERGY.2015.05.103.
[65] M. P. Mercer, C. Peng, C. Soares, H. E. Hoster, and D. Kramer, “Voltage hysteresis during lithiation/delithiation of graphite associated with meta-stable carbon stackings,” *Journal of Materials Chemistry A*, vol. 9, no. 1, pp. 492–504, Jan. 2021, doi: 10.1039/D0TA10403E.
[66] M. A. Roscher, O. Bohlen, and J. Vetter, “OCV Hysteresis in Li-Ion Batteries including Two-Phase Transition Materials,” *International Journal of Electrochemistry*, vol. 2011, pp. 1–6, 2011, doi: 10.4061/2011/984320.
[67] H. Konishi, T. Hirano, D. Takamatsu, A. Gunji, X. Feng, and S. Furutsuki, “Origin of hysteresis between charge and discharge processes in lithium-rich layer-structured cathode material for lithium-ion battery,” *Journal of Power Sources*, vol. 298, pp. 144–149, Dec. 2015, doi: 10.1016/J.JPOWSOUR.2015.08.056.
[68] Y. Zhu and C. Wang, “Strain accommodation and potential hysteresis of LiFePO4 cathodes during lithium ion insertion/extraction,” *Journal of Power Sources*, vol. 196, no. 3, pp. 1442–1448, Feb. 2011, doi: 10.1016/J.JPOWSOUR.2010.08.008.
[69] B. Lu, Y. Song, Q. Zhang, J. Pan, Y. T. Cheng, and J. Zhang, “Voltage hysteresis of lithium ion batteries caused by mechanical stress,” *Physical Chemistry Chemical Physics*, vol. 18, no. 6, pp. 4721–4727, Feb. 2016, doi: 10.1039/C5CP06179B.
[70] P. Yu, S. Wang, C. Yu, W. Shi, and B. Li, “Study of hysteresis voltage state dependence in lithium-ion battery and a novel asymmetric hysteresis modeling,” *Journal of Energy Storage*, vol. 51, p. 104492, Jul. 2022, doi: 10.1016/J.EST.2022.104492.
[71] J. P. Christopherson, “Battery Test Manual For Electric Vehicles,” 2015.
[72] L. A. Middlemiss, A. J. R. Rennie, R. Sayers, and A. R. West, “Characterisation of batteries by electrochemical impedance spectroscopy,” *Energy Reports*, vol. 6, pp. 232–241, May 2020, doi: 10.1016/j.egyr.2020.03.029.
[73] K. E. Thomas, C. Bogatu, and J. Newman, “Measurement of the Entropy of Reaction as a Function of State of Charge in Doped and Undoped Lithium Manganese Oxide,” *Journal of The Electrochemical Society*, vol. 148, no. 6, p. A570, Jun. 2001, doi: 10.1149/1.1369365/XML.
[74] K. Jalkanen, T. Aho, and K. Vuorilehto, “Entropy change effects on the thermal behavior of a LiFePO 4/graphite lithium-ion cell at different states of charge,” *Journal of Power Sources*, vol. 243, pp. 354–360, 2013, doi: 10.1016/j.jpowsour.2013.05.199.
[75] D. Allart, M. Montaru, and H. Gualous, “Model of Lithium Intercalation into Graphite by

Potentiometric Analysis with Equilibrium and Entropy Change Curves of Graphite Electrode," *Journal of The Electrochemical Society*, vol. 165, no. 2, pp. A380–A387, Feb. 2018, doi: 10.1149/2.1251802JES/XML.

[76] Y. Reynier, R. Yazami, and B. Fultz, "The entropy and enthalpy of lithium intercalation into graphite," *Journal of Power Sources*, vol. 119–121, pp. 850–855, Jun. 2003, doi: 10.1016/S0378-7753(03)00285-4.

[77] G. K. Mertin *et al.*, "On the possible influence of the Fermi–Dirac statistics on the potential and entropy of galvanic cells," *Journal of Power Sources*, vol. 498, p. 229870, Jun. 2021, doi: 10.1016/J.JPOWSOUR.2021.229870.

[78] C. Wang, C. Li, G. Wang, C. Zhang, and N. Cui, "Fast identification method for thermal model parameters of Lithium-ion battery based on discharge temperature rise," *Journal of Energy Storage*, vol. 44, p. 103362, Dec. 2021, doi: 10.1016/J.EST.2021.103362.

[79] T.-H. Tran, S. Harmand, B. Desmet, and F. Pailhoux, " Thermal Characterization of LiNi 0.8 Co 0.15 Al 0.05 O 2 /Graphite Battery ," *Journal of The Electrochemical Society*, vol. 160, no. 6, pp. A775–A780, 2013, doi: 10.1149/2.044306jes.

[80] G. K. Mertin *et al.*, "Dynamic measurement of the entropy coefficient for battery cells," *Journal of Energy Storage*, vol. 51, Jul. 2022, doi: 10.1016/J.EST.2022.104361.

[81] Y. Hu, S. Y. Choe, and T. R. Garrick, "Hybridized time-frequency method for the measurement of entropy coefficient of lithium-ion battery," *Electrochimica Acta*, vol. 362, 2020, doi: 10.1016/j.electacta.2020.137124.

[82] F. Yun, W. Jin, L. Tang, W. Li, J. Pang, and S. Lu, " Analysis of Capacity Fade from Entropic Heat Coefficient of Li[Ni x Co y Mn z]O 2 /Graphite Lithium Ion Battery ," *Journal of The Electrochemical Society*, vol. 163, no. 5, pp. A639–A643, 2016, doi: 10.1149/2.0311605jes.

[83] J. R. Dahn, "Phase diagram of Li_xC_6," *Physical Review B*, vol. 44, no. 17, pp. 9170–9177, 1991.

[84] A. F. Gunnarshaug, P. J. S. Vie, and S. Kjelstrup, "Review—Reversible Heat Effects in Cells Relevant for Lithium-Ion Batteries," *Journal of The Electrochemical Society*, vol. 168, no. 5, p. 050522, May 2021, doi: 10.1149/1945-7111/abfd73.

[85] Y. Ji, Y. Zhang, and C.-Y. Wang, "Li-Ion Cell Operation at Low Temperatures," *Journal of The Electrochemical Society*, vol. 160, no. 4, pp. A636–A649, Feb. 2013, doi: 10.1149/2.047304JES/XML.

[86] G. Liu, M. Ouyang, L. Lu, J. Li, and X. Han, "Analysis of the heat generation of lithium-ion battery during charging and discharging considering different influencing factors," *Journal of Thermal Analysis and Calorimetry*, vol. 116, no. 2, pp. 1001–1010, Jan. 2014, doi: 10.1007/S10973-013-3599-9/FIGURES/10.

[87] C. Lin, S. Xu, and J. Liu, "Measurement of heat generation in a 40 Ah LiFePO4 prismatic battery using accelerating rate calorimetry," *International Journal of Hydrogen Energy*, vol. 43, no. 17, pp. 8375–8384, Apr. 2018, doi: 10.1016/J.IJHYDENE.2018.03.057.

[88] M. Song, Y. Hu, S.-Y. Choe, and T. R. Garrick, "Analysis of the Heat Generation Rate of Lithium-Ion Battery Using an Electrochemical Thermal Model," *J. Electrochem. Soc.*, vol. 167, no. 12, p. 120503, Aug. 2020, doi: 10.1149/1945-7111/aba96b.